Geostratigraphic mapping of the intrusive Valentine Domes on the Moon

Javier Eduardo Suárez-Valencia[1], Angelo Pio Rossi[2]

[1]Constructor University, Bremen, Germany.

[2]Earthgraph

Corresponding author: Javier Eduardo Suarez-Valencia (jsuarezvalencia@constructor.university)

This manuscript is an article published in the Journal of Geophysical Research: Planets.

Abstract

Lunar intrusive igneous domes have not been the center of much research in the past due to their rare occurrence on the lunar surface, and the difficulty in locating them. Most of the known structures were discovered using images with low illumination angles, including data from the Lunar Orbiter, telescopic images, and photos taken during the Apollo Missions. These intrusive domes are characterized by an oval shape and low slopes. We analyzed one of these systems, the Valentine domes, located near the rim of the west Serenitatis basin with modern techniques and datasets from the Lunar Reconnaissance Orbiter (LRO) and Chandrayaan-1 missions. We created a geostratigraphic map of the area, combining geomorphological and spectral classifications. The aspect map (direction of the slope) proved to be the most suitable product to locate and delimit these structures; using it, we identified a new dome southeast of the principal body, suggesting that the intrusive system is larger than previously thought. It was found that the three domes can be classified as laccoliths; and that several secondary structures such as rilles, dykes, and secondary domes represent different stages of intrusive activity in the area. Based on crater counting analysis, we determined that the intrusive activity began after 2.98 ± 0.15 Ga and lasted at least until 1.88 ± 0.5 Ga ago.

Plain Language Summary

Igneous intrusive domes have not been extensively studied, in part due to their rare occurrence on the lunar surface. In this work, we used data derived from the Lunar Reconnaissance Orbiter (LRO) and Chandrayaan-1 to analyze and construct a comprehensive map of the Valentine Domes system near the rim of the Serenitatis basin, a group of small hills formed from the cooling and emplacement of magma below the surface. This type of domes are difficult to identify from satellite imagery due to its subtle effect on the topography, but using modern datasets, we discovered a new dome, while also studying those that are already known. The detailed mapping allowed us to identify several smaller structures around the main domes, which proved the system is more complex and bigger than previously thought. Our analyses suggest that the igneous system was active at least until 1.8 Ga ago.

1 Introduction

Lunar geological activity has been largely dominated by igneous and impact-related processes (e.g., Shearer et al., 2023). Large impacts were responsible for the formation of the observed major basins, as well as the generation of large amounts of ejecta and their subsequent accumulation in the surrounding areas (e.g., Geiss and Rossi, 2013; Liu et al., 2021). Extrusive igneous processes have also played a major role in the present geology of the Moon, creating the vast fields of basaltic materials called maria (e.g., Taylor, 2007). Other expressions of extrusive activity include large volcanic complexes, such as Mons Rümker (e.g., Scott and Eggleton, 1973; Zhao et al., 2017) or Marius Hills (e.g., McCauley 1967; Huang et al., 2011), but several small-scale landforms dominate the diversity of lunar volcanism. Lunar rilles carved by lava flows are commonly found in the maria (Garfinkle 2020), and in some cases, they are associated with pits of high scientific interest (Wanet and Robinson 2014). Less common are pyroclastic deposits, which can be related to cinder cones or fractures in the surface (Gustafson et al., 2012). Extrusive magmatism even plays a role in small-scale features, like the rim-moat structures common in the lunar maria, which were probably formed in the last stages of maria formation

(Zhang et al., 2017). Although the extent of extrusive igneous activity on the lunar surface is substantial as seen in the previous examples, this is not true for intrusive igneous processes.

1.1 Intrusive rocks on the Moon

The absence of widespread intrusive bodies on the lunar surface is related to the mechanisms of intrusive activity itself. The ascent of magmatic bodies that cooled under the surface is controlled by the buoyancy of both the intrusion and the host rock, and the distribution of stress in the crust (Wilson and Head, 2017). In contrast to Earth, on the Moon there is no widespread mechanism such as crustal contamination that allows magma originating from the mantle to evolve and overcome their density difference with the lighter upper crust (e.g., Shearer et al., 2006, Wieczorek et al., 2006). This impedes the rise of the magma, consequently, the intrusive bodies tend to lose heat and stall within the lower crust (e.g., McCallum and Schwartz, 2001). Nevertheless, some rock fragments among the samples returned during the Apollo, Luna, and Chang'e-5 missions have been interpreted as intrusive in origin (e.g., Papike et al., 1998, Zhang et al., 2021; Laul and Schmitt, 1973). Two distinct groups of rocks were identified, the Mg-suite, characterized by the presence of silicates with high contents of magnesium (Shearer et al., 2015); and the Al-suite, enriched in alkaline elements and with significant concentrations of rare earth elements (Snyder et al., 1995). The named samples were found both as complete fragments or as small aggregates in lunar breccias, and an estimated crystallization depth of 40-50 km was constrained for the Mg-Suite (Shearer et al., 2015).

There are only two routes through which these fragments (or any other intrusive body) may have reached the lunar surface. Either by the mechanical exhumation of intrusive bodies from the lower crust or by their intrusion into regions where the crust was thin. Both instances could have resulted from large impacts on the lunar surface (**Figure 1**). Numerical simulations suggest that the largest impacts on the Moon could have excavated materials as deep as the mantle (e.g., Miljković et a., 2015). Through this process, rocks of the Mg-suite and Al-suite would have been scattered on the surface as ejecta or enclosed in the structurally uplifted central peaks of complex craters (Klima et al., 2011, Bretzfelder et al., 2020). Another outcome of large impacts was the thinning and fracturing of the crust, which could create conduits where magma from the mantle ascends, erupts, and infills the craters (Hartmann and Wood, 1971). This induced magmatism would also produce small and relatively shallow intrusions such as dykes and laccoliths (Head and Wilson, 2017). Due to this formation process, these intrusions have been found mostly within maria. Dykes and related geological features can also be commonly found in maria, either directly on the surface as linear or sinuous ridges, or generating other structures when stalled near it, such as linear grabens or aligned cinder cones (Head and Wilson, 2017).

Intrusive domes are less common since only a handful have been identified, mainly by Whöler et al. (2009) and Lena et al. (2013). Individual domes have not been studied in detail before this work, mainly due to their subtle effect on the surface and the difficulty in locating them. These structures are interesting due to their morphology and the geologic processes associated with their emplacement on the lunar surface. New data have been obtained since the work done by Lena et al. (2013), allowing a high-resolution analysis of these structures, which is important for improving our understanding of their formation. In this work, we carried out a geostratigraphic analysis of the Valentine Domes region (30.69° N, 10.20° E), which allowed us to interpret their origin and infer the properties of lunar intrusive domes in a broader context. We chose to study the Valentine Domes due to their complex manifestation at the surface. There are several small-scale mounds and fractures near or inside the domes, which is not the case for the other candidates located by Lena et al. (2013). These features suggest that the intrusive system had further effects on the surface beyond the formation of the laccolith, which does not seem to be the case for other lunar intrusive domes.

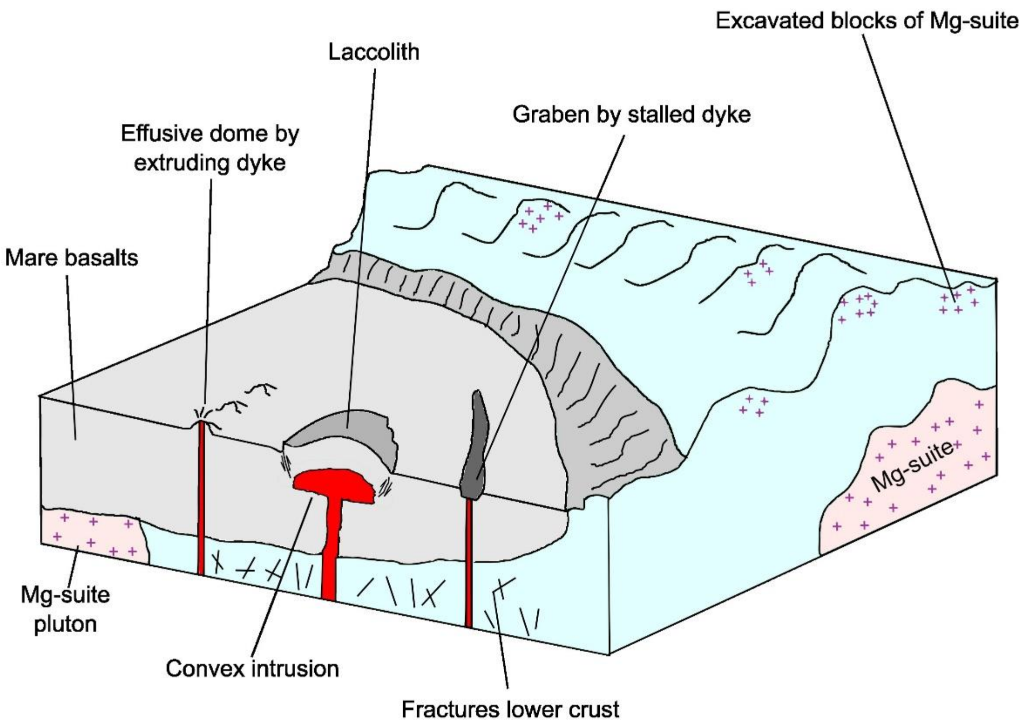

Figure 1: Sketch representation of the two possible processes that can result in the emplacement of intrusive igneous rocks on the surface: first, by large impacts that can exhume intrusive rocks from the lower crust and deposit them as ejecta on the rim of lunar impact basin; or second, as induced magmatism generated in large basins due to the thinning of the crust, expressed on the surface as laccoliths/intrusive domes (figure not to scale).

1.2 Intrusive domes on the Moon

Lena et al. (2013) defined 16 candidate intrusive domes using telescopic pictures and images from the Wide Angle Camera (WAC) onboard the Lunar Reconnaissance Orbiter (LRO) (Robinson et al., 2010). These structures can be differentiated from effusive domes because they do not have summit or lateral vents, nor lava flows associated with them. Additionally, they are typically wider, shorter, and more oval-shaped than other types of domes. These properties make them difficult to locate in optical or spectral images since they do not create an abrupt change in the topography or the composition of the surface. This is especially true for images in the visible range of the maria, where the opaque tones of the basaltic lavas can obscure shallow and wide structures like intrusive domes. These domes typically behave as laccoliths, which are convex-shaped uplifts made of pre-existing basaltic lavas, deformed by intruding plutons that stalled near the surface (Schofield et al., 2021). Lena et al. (2013) used the method of Kerr and Pollard (1998) to calculate the depth of the intrusions, obtaining values between 0.5 and 1 km. All the candidate intrusive domes occur on maria or transitional areas, and none are found in the highlands. This suggests that they are not fragments of the basement trapped in the mare, but rather structures formed from intruding magma (Lena et al., 2013).

1.3 Valentine Domes

The Valentine Domes are located in the northwestern region of Mare Serenitatis (30.69 N, 10.20 E), near the rim of the basin (**Figure 2**). The system was originally mapped as volcanic in origin by Hackman (1996). However, it was later described as a possible intrusive system by Whöler and Lena (2009), consisting of a main dome with a diameter of 30 km (V1), and a second dome to the north, with a diameter of 11 km (V2). Both were classified as laccoliths. These authors also derived a Digital Elevation Model (DEM) from telescopic images, from which they measured a maximum altitude of 130 m for V1 and 80 m for V2. Lena et al. (2013) highlighted two linear structures on V1, a fault that uplifts the east margin of the dome, and a rille that cuts the structure with an NW-SE trend. According to the global geological map of

Fortezzo et al. (2020), both domes are located within Eratosthenian lavas, younger than the Imbrian lavas that dominate the center of the Serenitatis Basin.

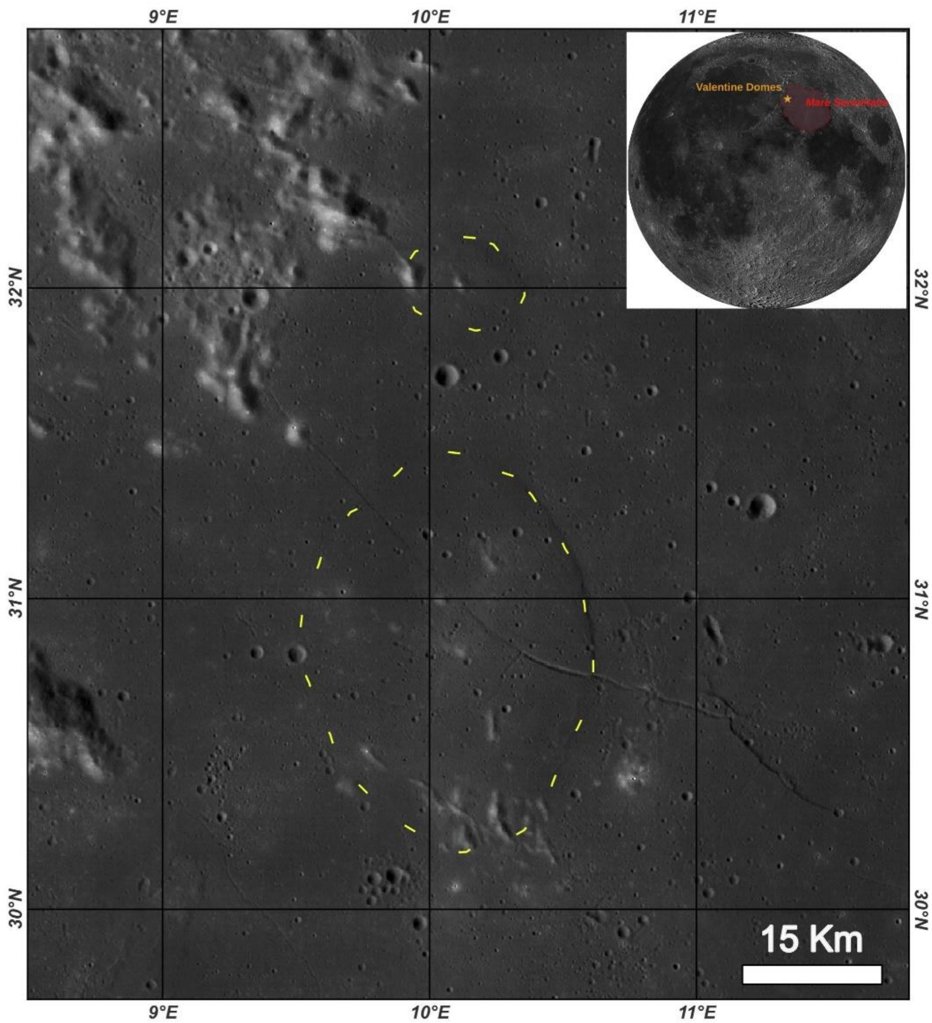

Figure 2: Location of the Valentine domes near the rim of the Mare Serenitatis (30.69° N, 10.20° E). The image is centered in the main dome (V1), which is an oval-shaped structure 30 km in diameter. To the north lies the smaller secondary dome V2, 11 km in diameter.

2 Data

Prior studies mainly used telescopic data and images from the Apollo missions since they could feature low illumination angles, thus generating large shadows and contrasts that allowed them to more confidently define the shape of the domes. Newer and more diverse datasets have become available since then, which we employed to analyze the domes at a high spatial resolution. We utilized two types of panchromatic images, both obtained by the LRO spacecraft. The first dataset was the global WAC mosaic produced by Speyerer et al. (2011), with a spatial resolution of 100 m/px, and the second dataset were images from the Narrow Angle Camera (NAC). We obtained 23 images from the Planetary Data System (PDS) (Robinson, 2009), and then created a high-resolution mosaic of the area with a horizontal spatial resolution of 3 m/px.

We also used two DEMs with different resolutions, the global LRO (LOLA)-Kaguya (LALT) mosaic produced by Barker et al. (2016), with a resolution of 59 m/px; and a DEM derived from NAC stereo pairs, with a spatial resolution of 3 m/px. To interpret the composition of the surface we generated spectral indexes derived from hyperspectral data obtained by the Moon Mineralogy Mapper (M^3) onboard Chandrayaan-1 (Green et al., 2011). The data cube had a spatial resolution of 110 m/px and contained 85 channels covering the 430 nm-3000 nm spectral range. The cube was downloaded from the PDS (Malaret, 2011). Since plagioclase is not easily recognized from M^3 data, we also used the global Christiansen Feature map from Lucey et al. (2021), derived from the Diviner Lunar Radiometer Experiment onboard LRO. The Christiansen feature is a position of minimum reflectance and maximum emission of certain silicates in the thermal infrared range, which is particularly useful for identifying plagioclase since its absorption features do not overlap with those of pyroxene and olivine, as it occurs in the near-infrared range. Finally, we analyzed the Bouguer gravitational anomalies derived from GRAIL, using the basemaps developed by Goossens et al. (2021). A list of all the products used in this work can be found in **Table S1**.

3 Methods

3.1 Data correction and projection

Data derived from other authors were ready to analyze, but the NAC images and the M^3 cube needed further processing. Both products were converted to map-projected images using the Integrated Software for Imagers and Spectrometers (ISIS) (Laura et al., 2023) and the Geospatial Data Abstraction Library (GDAL) (Rouault et al., 2023). The processing of NAC images included importing to ISIS, a radiometric correction, a noise correction, the map projection, and finally, the generation of a TIF file usable in geospatial software. The processing of M^3 cubes was more convoluted, the importing command of ISIS only accepts the radiance product of M^3, so we modified the associated LBL file of the radiance cube to use the reflectance data (Figuera et al., 2018). Following these steps, the map projection and format transformation were completed successfully. A detailed description of the scripts used in this process can be found in **Text S1**.

2.2 Derived products

We found that a better understanding of the shape of the domes could be achieved by studying the DEMs and derivative products. The spatial resolution of the LRO-Kaguya DEM is not high enough to define small structures, so we created a stereo DEM using the Ames Stereo Pipeline (ASP) (Beyer et al., 2018). We used five overlapping NAC images to generate a DEM that covered the entire area. We created three more terrain products derived from both DEMs using the geospatial software QGIS: a hillshade, a slope map, and an aspect map (**Figure 3**), they were made with the homonymous tools of QGIS. These products greatly enhanced the morphology of the domes and the landforms on top of them, but the aspect map was especially useful in delimiting the boundaries of the domes. This is because the aspect parameter features the azimuth direction of the slope, regardless of its magnitude, so the limits of the domes are visible even when the slope is low (Florinsky, 2012).

We also derived 28 spectral indexes from the M^3 cube to complement the classification of geological units (**Table S2**). This process was carried out using the Python library ***MoonIndex*** (Suárez-Valencia et al., 2024), which takes the map-projected cube as input and performs the filtering, the removal of the continuum, and then generates a set of spectral indexes aimed at characterizing mineralogy. These spectral indexes are focused on highlighting the properties of the absorption bands around 1 µm and 2 µm, since they record the interaction between the mafic minerals common on the lunar surface: olivine, clinopyroxene and orthopyroxene. Other indexes use mathematical operations on certain bands to showcase the presence of other minerals or compounds, like spinel, iron oxide, or anorthosite. (Suarez-Valencia et al., 2024). We also used spectral signatures after the continuum removal to discuss specific differences between certain structures. In this work we used the convex hull continuum-removal method (Graham, 1972).

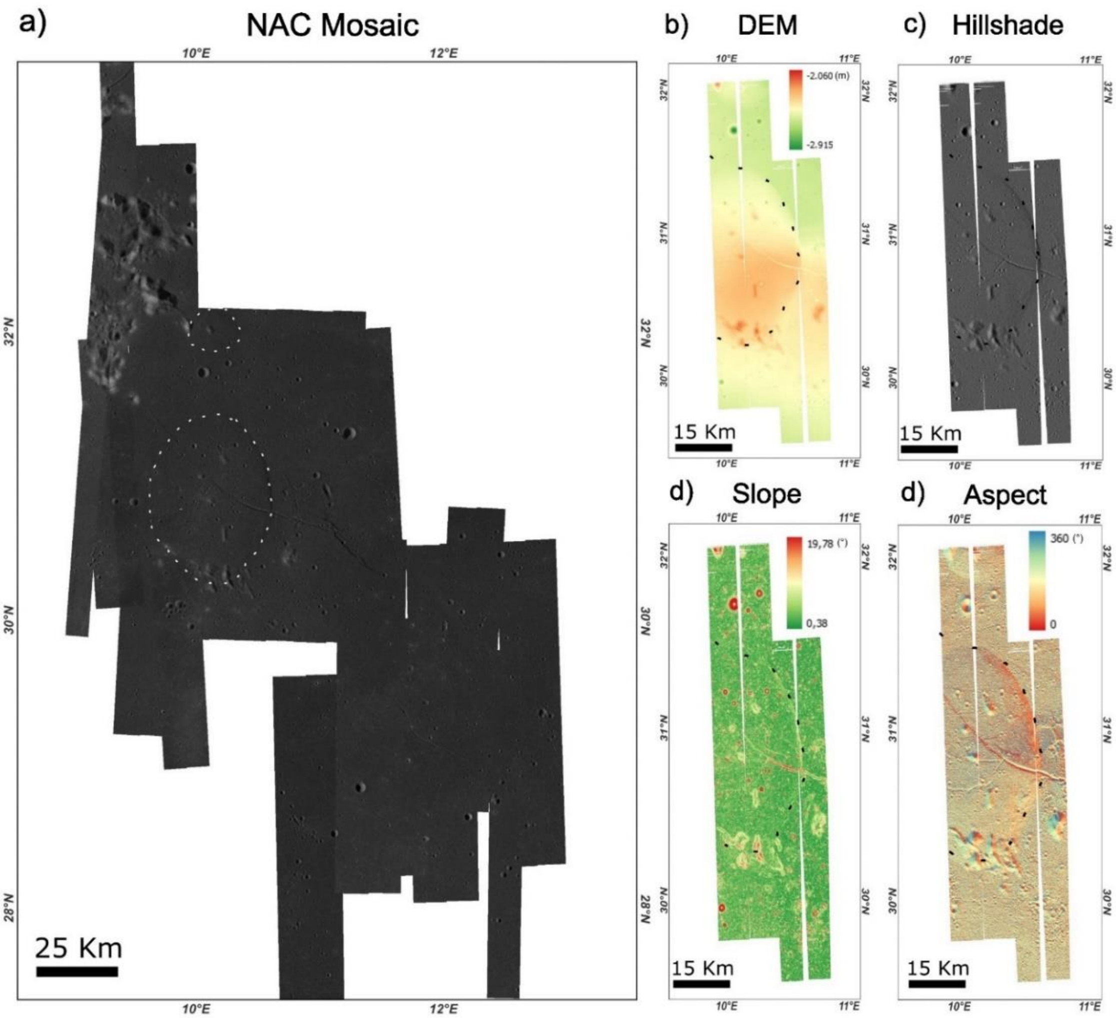

Figure 3: Detailed datasets used to create the geomorphological map. a) Mosaic of NAC images of the area, b) DEM of the area derived from NAC stereo pairs images, c) Hillshade

derived from the DEM, d) Slope derived from the DEM, e) Aspect derived from the DEM, the dome is especially clear in this product.

2.3 Mapping techniques

To characterize the Valentine domes in detail, we decided to map them at two scales. On a regional level, we focused on establishing relationships between the major domes and rilles and how they fit in the geological configuration of the Serenitatis basin rim. At the detailed scale, we mapped just the domes and their surroundings, since several secondary and small landforms lie within them, and are key to understanding the evolution of the intrusive system. We used a hybrid approach to define the units on the map (e.g., Canale et al., 2023; Yingst et al., 2023; Massironi et al., 2021). In this method, the final map is a combination of previous geomorphological and spectral maps, defined by a categorized tree of decisions (Yingst et al., 2023). Instead of combining two maps, we decided to define geomorphological units first, which were later refined or modified according to the spectral information (Fassett and Head, 2008; Wright et al., 2024; Tognon et al., 2024). We followed this approach since in our case the resolution of the panchromatic data is more than ten times higher than the spectral information; also, it would be impractical to create a single spectral map or several maps for each one of the 28 indexes. Finally, we also added relative ages to the units. For the smallest units this was done by analyzing cross-cutting relationships, and for the larger ones the age was defined using the crater size-frequency counting technique (Neukum et al., 2001), and with the updated chronology model of Yue et al. (2022). We also performed a buffer crater-counting analysis to study the relationship between the larger rilles and the domes (Kneissl et al., 2014). The analysis and mapping of the data were carried out in the geoprocessing software QGIS with the aid of the Mappy plug-in (Penasa, et al., 2023), the crater counting was performed with the CraterTools extension of ArcGIS (Kneissl et al., 2011), and the age determination in the Python version of the software CraterStats (Michael, 2021).

4 Results

We first present the regional mapping, which allowed us to identify large-scale trends of the underlying magmatic bodies and other surficial structures not identified by previous authors. We then move to the detailed mapping of the domes, which records the specific properties of the laccoliths and defines the stratigraphic relationships between the different intrusive pulses of the system. The complete maps at both scales can be seen in **Figures S4 and S5**.

4.1 Regional setting

The greatest morphological contrast in the area occurs between the rim and the mare of the Serenitatis basin. The rim has high albedo, scarped topography, and a dominant abundance of plagioclase, according to the map of Lucey et al. (2021) (**Figure S1**). In contrast, the mare is dark toned, has a smooth texture, and does not show a detectable signal of plagioclase; this is the result of a major abundance of mafic minerals, which can mask the signal of plagioclase even if it is present (Arnold et al., 2016). However, the small-scale mounds inside V1 do have a higher signal of plagioclase, probably due to a smaller amount of mafic minerals. We also checked the Bouguer gravitational anomaly using the map of Goossens et al. (2021), and although we found a strong positive anomaly beneath the mare, there is a ring-like structure with a lower anomaly near the intrusive domes (**Figure S2**). The GRAIL spatial resolution does not allow a detailed analysis of this feature, but its origin might be related to a buried impact crater.

4.1.1 New dome

As mentioned in the previous section, locating the intrusive domes is not a straightforward process. Using the aspect map derived from the Kaguya DEM we were able to recognize a new dome (V3) (**Figure 4, Figure 5**). It has a diameter of 43 by 33 km, making it the biggest dome of the Valentine system (**Figure 4 a,b**). V3 is oval-shaped and asymmetric, its eastern flank is more pronounced than the western one, but it does not have a steep scarp like V1. The emplacement of this dome had little effect on the surface, as the only noticeable feature in the mare is a narrow linear rille that crosses the dome in an NW-SE direction (**Figure 4**). V3 has a gentle slope of 0.43°, compared to the 4.3° of V1, which might be the reason why it was not identified by Lena et al. (2013).

Another interesting feature lies between V1 and V3, the last segment of the long linear rille that dissects V1 since it is slightly uplifted in comparison to the rest of the rille. In the aspect map, a linear bump crosses the rille with an NE-SW trend, like the main wrinkle ridges in the area (**Figure 4a**). Nevertheless, the feature does not resemble a wrinkle ridge, since it is wider and their edges are not sinuous. We interpret this structure as an incipient uplift generated by another intrusive body. Its shape is irregular, and its borders are diffuse, so we classified it as an incipient dome (**Figure 5**). After locating these new structures, we evaluated their relationships with the developed domes V1 and V2. Using the Kaguya DEM and the aspect map, we observed a slight bump in the mare that encloses V1, V3, and the incipient dome (**Figure 4a, c**). The affected area of the mare spans more than 2700 Km^2.

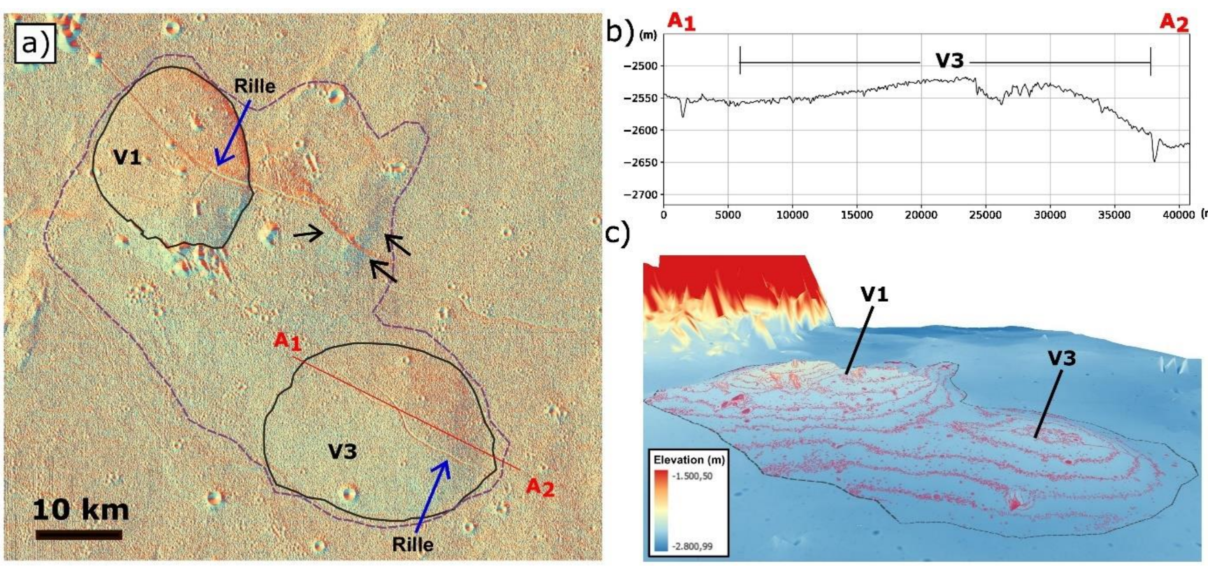

Figure 4: Total area affected by the Valentine intrusive system. a) Location of the newly discovered V3, the largest dome of the three. It has a limited effect on the overall surface topography. The black arrows point to the incipient dome, and the blue arrows to the rilles

cutting the domes. b) Profile of V3, the dome is asymmetric, having a steeper slope to the east. c) 3D view of the area, showing the upwelled mare around the two larger domes.

4.1.2 Regional geostratigraphic mapping

The regional geostratigraphic map can be seen in **Figure 5** (1:100,000 scale). Because of its location at the rim of the Serenitatis basin, the area is largely dominated by highlands and mare units. The igneous units related to the intrusive system are concentrated towards the middle of the area and will be analyzed further in the detailed mapping section.

4.1.2.1 Highlands/rim units

The highlands units make up the rim of the basin, which are characterized by an elevated topography, bright color in optical data, a strong signal of plagioclase in the Christiansen feature (**Figure S1**), and the relative absence of mafic minerals in the spectral indexes derived from M^3 (**Figure 6a**). The most extended unit is represented by Hilly materials (***Ihim***), characterized by an abrupt topography and blocky appearance. The main mineral signature is anorthosite, but some escarps suggest the presence of olivine in the olivine-detecting index (**Figure 6b**). This unit probably originated as part of the impact ejecta linked to the formation of the basin. The other unit in this group is Hummocky material (***Ihum***), which is differentiated from ***Ihim*** only by its lower topography and a more hummocky texture. According to the global map of Fortezzo et al. (2019), both units are Imbrian in age, although they may be older.

An additional highlands unit is represented by Kipuka (***Ik***), which refers to blocks of highlands material that were embedded by mare units, like islands, so their optical and compositional properties are the same as other highlands units. Whöler and Lena (2009) classified all the structures inside and around V1 as kipukas, but in this work, we separate them between kipukas and secondary intrusive domes.

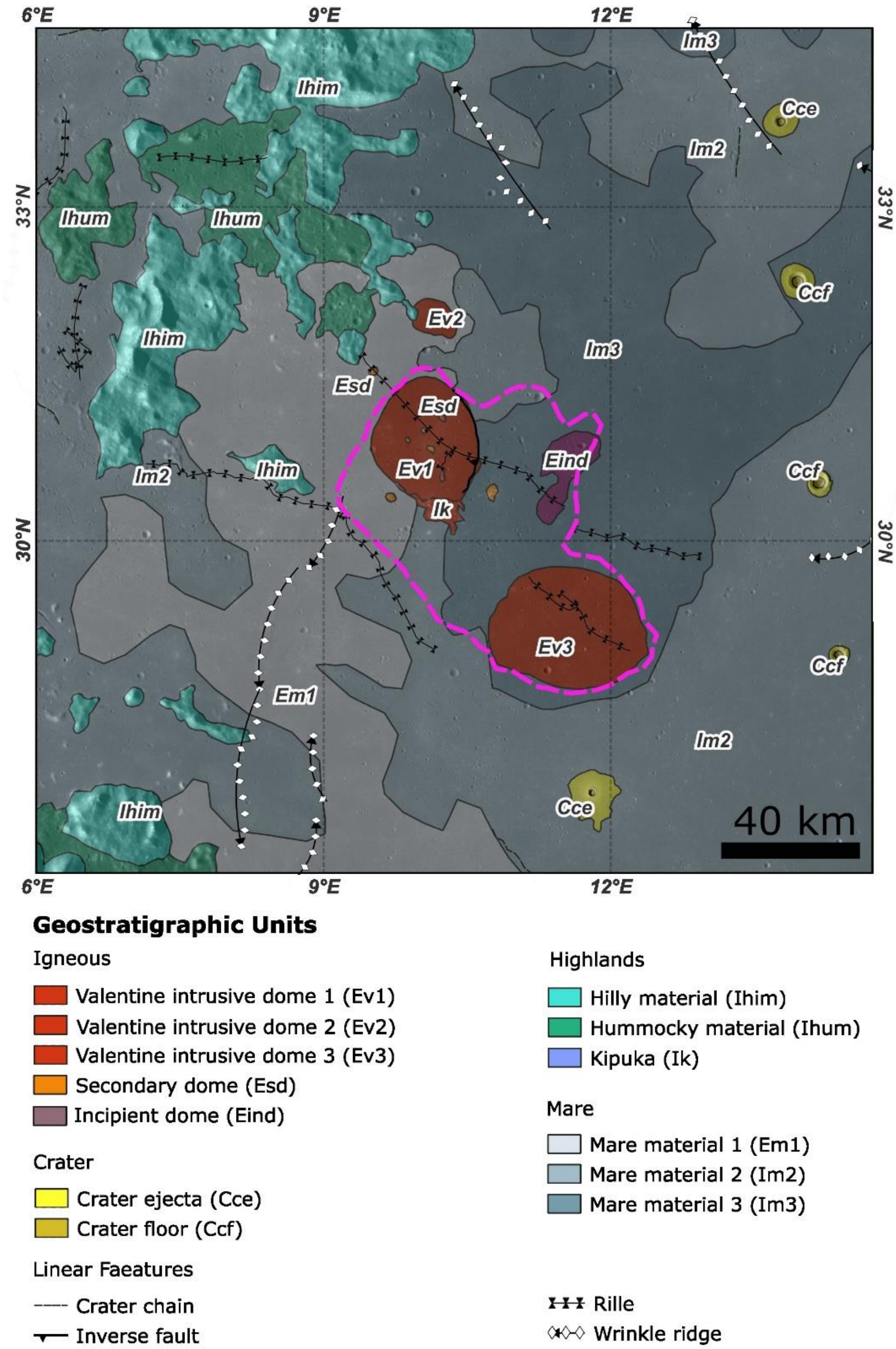

Figure 5: Regional geostratigraphic map of the region. The total area affected by the main uplift from the intrusive dome is outlined in pink. The basemap is a global WAC mosaic (Speyerer et al., 2011).

4.1.2.2 Mare units

The mare units in the area represent three different phases of lava flooding, which together are the most extensive units in the study area. Although the intrusive domes were mapped as distinct units for clarity, it is important to mention that the intrusive rocks most likely did not reach the surface, so the mare units represent the actual composition of the domes at the surface.

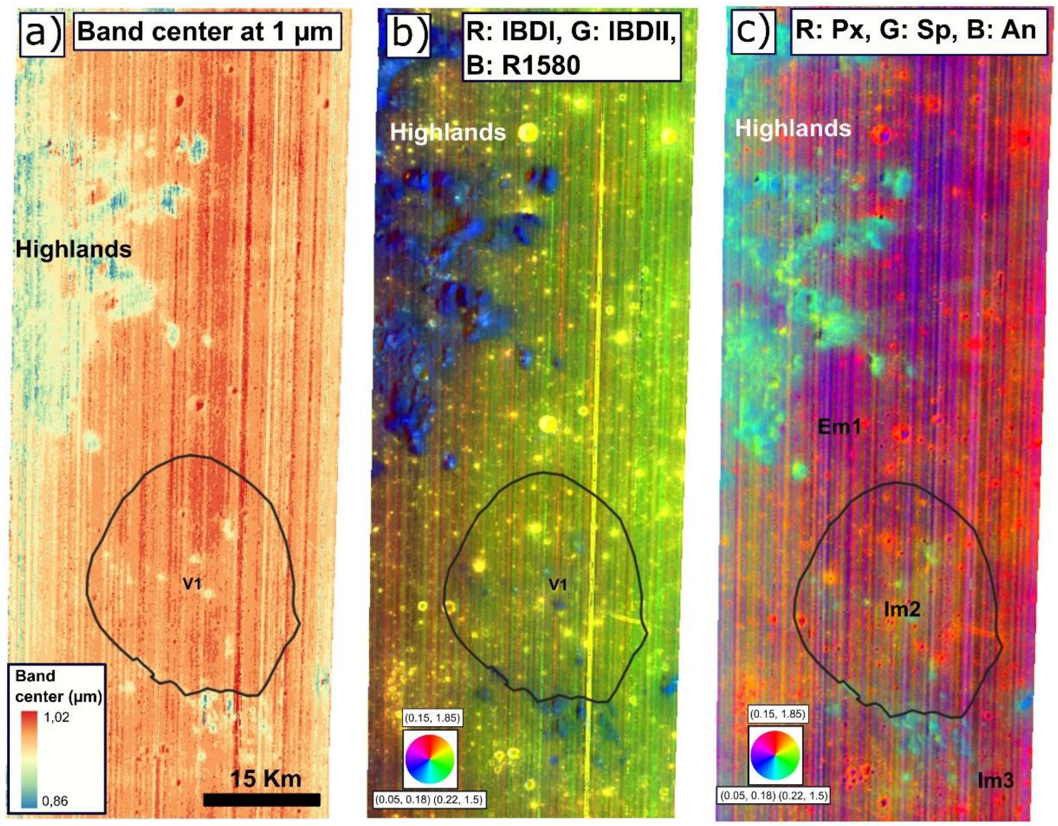

Figure 6: Spectral indexes used in this work. a) Band center at 1 μm, longer wavelengths suggest the presence of pyroxene and olivine. b) RGB composite highlighting the presence of anorthosite in blue, pyroxene in green, and olivine in red. c) RGB composite that highlights pyroxene in red, spinel in green-yellow, and anorthosite in light blue.

Apart from some slight color changes, the three units are all dark-toned, flat, and have a smooth texture. Nevertheless, the phases show variations in composition and age, which were the criteria used to differentiate them. The younger unit is Mare material 1 (***Em1***), which is located on the western edge of the basin. It has an estimated age of 2.9 Ga according to Fortezzo et al. (2019) and Hiesinger et al. (2011), but we obtained instead an Absolute Model Age (AMA) of 2.59 ± 0.3 Ga, using the crater-counting method. Compositionally, it is dominated by a strong signal of mafic minerals (**Figure 6c**). The V2 dome is intruding below this unit, as well as the western part of V1. The unit Mare material 2 (***Im2***) differs from the other two due to a relatively higher concentration of spinel (**Figure 6c**). An AMA of 3.32 ± 0.1 Ga was estimated for this unit (**Figure 12**). This unit extends over most of the area on top of V1. Finally, the older flood basalt in the region is represented by Mare material 3 (***Im3***), this unit covers the northeast part of the area and it is spectrally similar to ***Em1***. We calculated an Absolute Model Age (AMA) of 3.66 ± 0.01 Ga for this unit (**Figure 12**), and it mantles the entire area of V3.

4.1.2.3 Craters units

All impact structures in the investigated location are either single simple craters or are arranged in crater chains (**Figure 5**). Single craters were mapped as two units: the crater floor (Copernican and Eratosthenian, ***Ccf, Ecf***) unit, and the crater ejecta (***Ece, Ece***) unit, when the latter was present. Crater chains were mapped as linear features on the regional scale due to resolution constraints, but as a crater chain (***Ecc***) unit in the detailed map. The relative age of the craters can be estimated by the apparent degradation of their rims and ejecta (Agarwal et al., 2019), therefore we classified the ones with clear and bright ejecta, and with a sharp rim, as recent, that is Copernican in age; and the ones without ejecta or/and with eroded rims as at least Eratosthenian in age, although they might also be Imbrian.

4.2 Detailed analysis

We analyzed high-resolution NAC images centered on the intrusive domes area, and we produced a detailed geostratigraphic map with a scale of 1:25,000 (**Figure 7**). At this scale, structures related to deformation are also more prominent, which led to a new classification of several volcano-tectonic units. Highlands, mare, and crater units are also represented in the area, so their definition is the same as in the regional mapping.

4.2.1 Volcano-tectonic units

We consider volcano-tectonic units to be those structures that were formed by deformation and fractures triggered by any kind of igneous activity (Azzaro et al., 2012). All the units are located inside the mare, so their composition is the same as the overlying lava flows. The most common volcano-tectonic units are wrinkle ridges (***Iwr***), which appear as elongated sinuous ridges inside the mare. Their origin has been attributed to the cooling of lava and the subsequent thermal contraction phase (Watters, 1988), which produced small ridges surrounded by thrust faults. Another common structure in the mare are grabens, linear depressions on the surface that can be formed by either stalled dykes or by extensional stress (Head and Wilson, 2017). Those created by the latter process were mapped as structural graben (***Isg***) units. Last, a pair of structural hills (***Ish***) were found close to the end of the rille that crosses V1, and next to an incipient dome (***Eind***) unit (**Figure 8a**). These hills are polygonal mesas that are surrounded by steep scarps. Their origin is probably related to the deformation produced by an underlying intrusion, consistent with their closeness to the incipient dome.

350

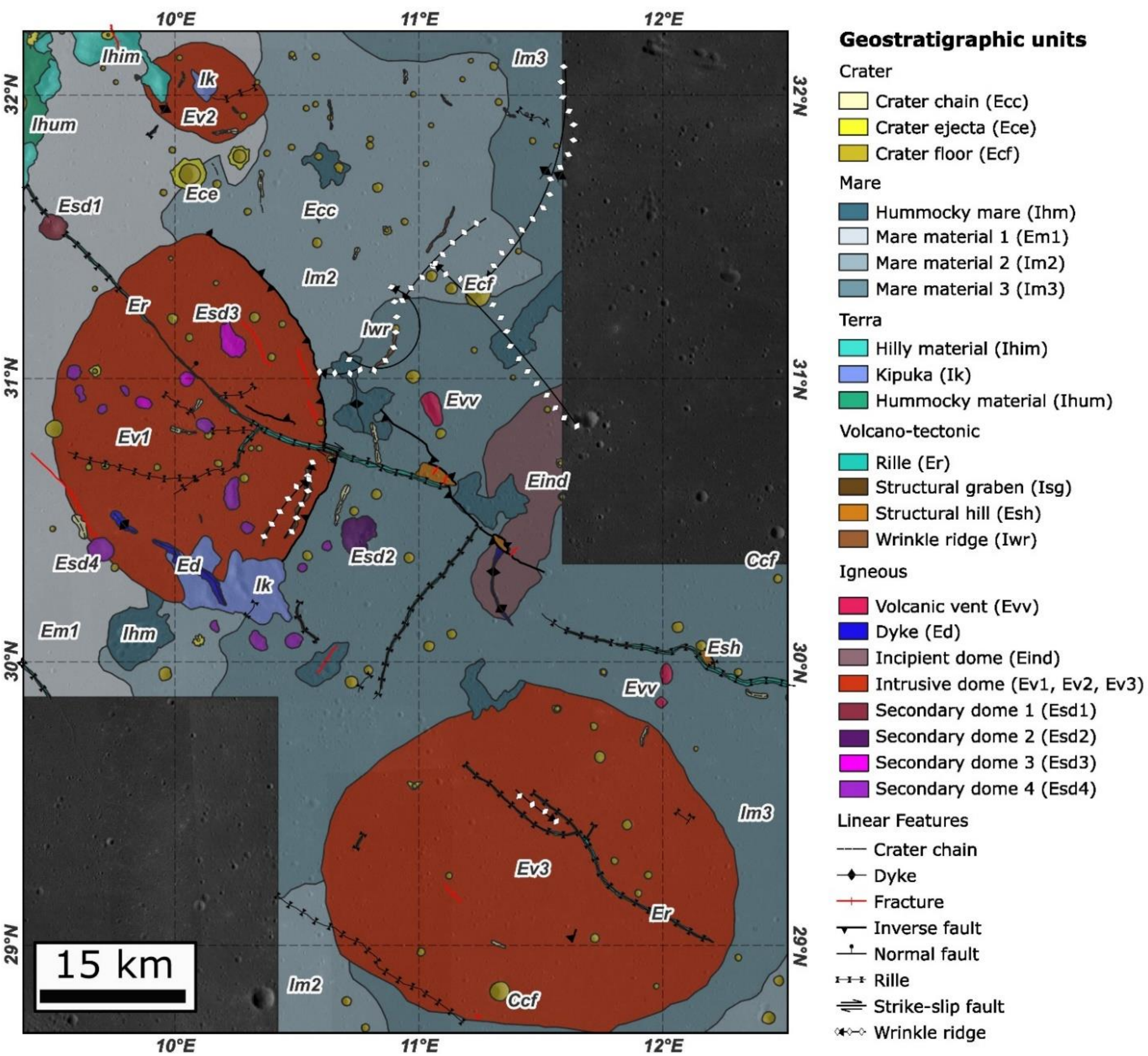

351 **Figure 7: Detailed geostratigraphic map of the area. The boudnaries of the mapped area correspond to the geographical extent**
352 **of the relevant NAC images.**

4.2.2 Igneous units

The igneous units in the area originated by both intrusive and extrusive activity. Among the extrusive ones, we found a few volcanic vents (***Evv***). These are irregular and oval structures, with gently elevated boundaries encircling an inner depression (**Figure 8b**). They are not spectrally distinct from the mare, and we found no anomalies in either the band area or band asymmetry at the 1 µm band, which is found in glass-bearing compositions (**Figure 9a, 9b**) (Horgan et al., 2014). This lack of contrast with the surrounding mare means that there are no recent pyroclastic deposits around the vents, indicating that they probably have not been active in recent geological times. Other extrusive features are dykes (***Ed***), which are vertical intrusions that reached the surface close to V1 and V2, creating linear ridges that cut across different mare units. Their spectral signature differs from those of the mare units, as the absorption features of the mafic minerals appear weaker, probably due to a lower concentration of these minerals or some variations in the maturity of these materials (**Figure 9c, 9d).** This type of spectral signature is common to other secondary structures found near the main domes. Dykes also influence the formation of rilles (***Er***), which represent grabens created by the extensional stress generated by a dyke that stalled near the surface (e.g. Head and Wilson, 2017). The larger rille in the area spans more than 50 km and runs from the rim of the basin to the ***Eind*** unit, crossing V1 and other secondary structures (**Figure 8c**). We also found a shorter rille (30 km) atop V3. The walls of the rilles have a similar spectrum to the mare, but the absorption of mafic minerals is considerably stronger (**Figure 9e, 9f**). This is the result of fresher materials and minerals being exposed by the rille.

Of the three main domes (***Ev2, Ev2, Ev3***), V1 and V2 contain several smaller structures on top of them. These structures were originally classified as kipukas by Whöler et al. (2009), but we found some that do not fit the description. A couple of actual kipukas (***Ik***) were located at the southern limit of V1 and in the middle of V2 (**Figure 10a**); they are characterized by an irregular shape and by having a spectral signature similar to the units in the highlands. The other structures were classified as secondary intrusive domes (***Esd1, Esd2, Esd3, Esd4***): they are round-shaped, aligned to each other, lie near the main rille, and none of them show a volcanic crater on the summit (**Figure 10b, 10c, 10d, 10e**). They are all located inside or near V1, and none around the other domes. The spectral signature of the exposed materials is similar to the highlands, but they show a higher band depth and a centering at longer wavelengths around the 1 µm band. Both parameters imply a higher abundance of mafic minerals compared to the rim units ***Ihum*** and ***Ihim*** (e.g. Adams, 1974; Klima et al., 2011).

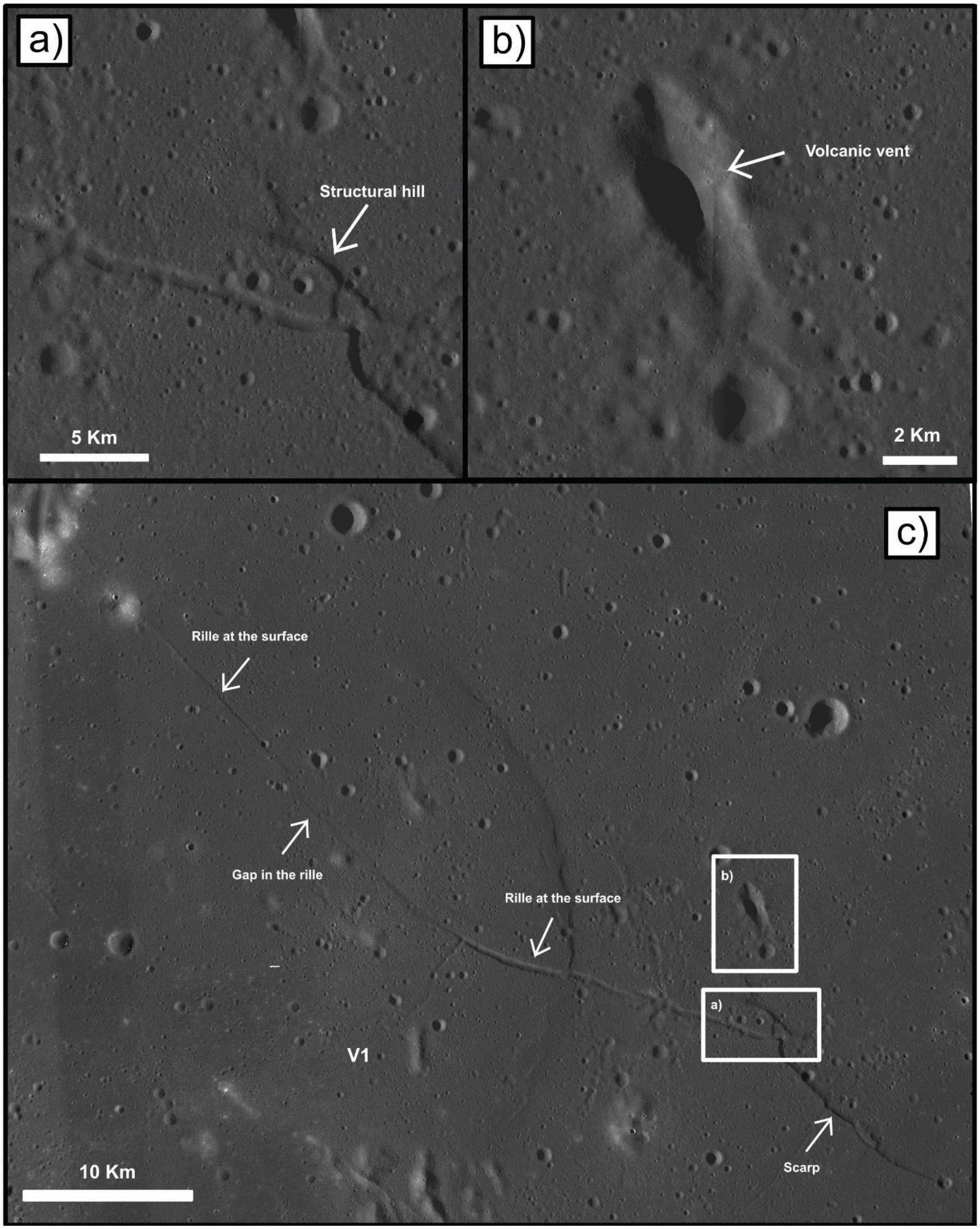

Figure 8: a) Structural hill, a polygonal structure at the end of the main rille. b) Possibly a volcanic vent, characterized by its elongated shape and the absence of a

defined rim. c) The largest rille in the area. It begins at the northwest corner of V1, disappears at its center, and reappears to the southeast. Once the rille ends, a scarp continues to the southeast for another 8 km.

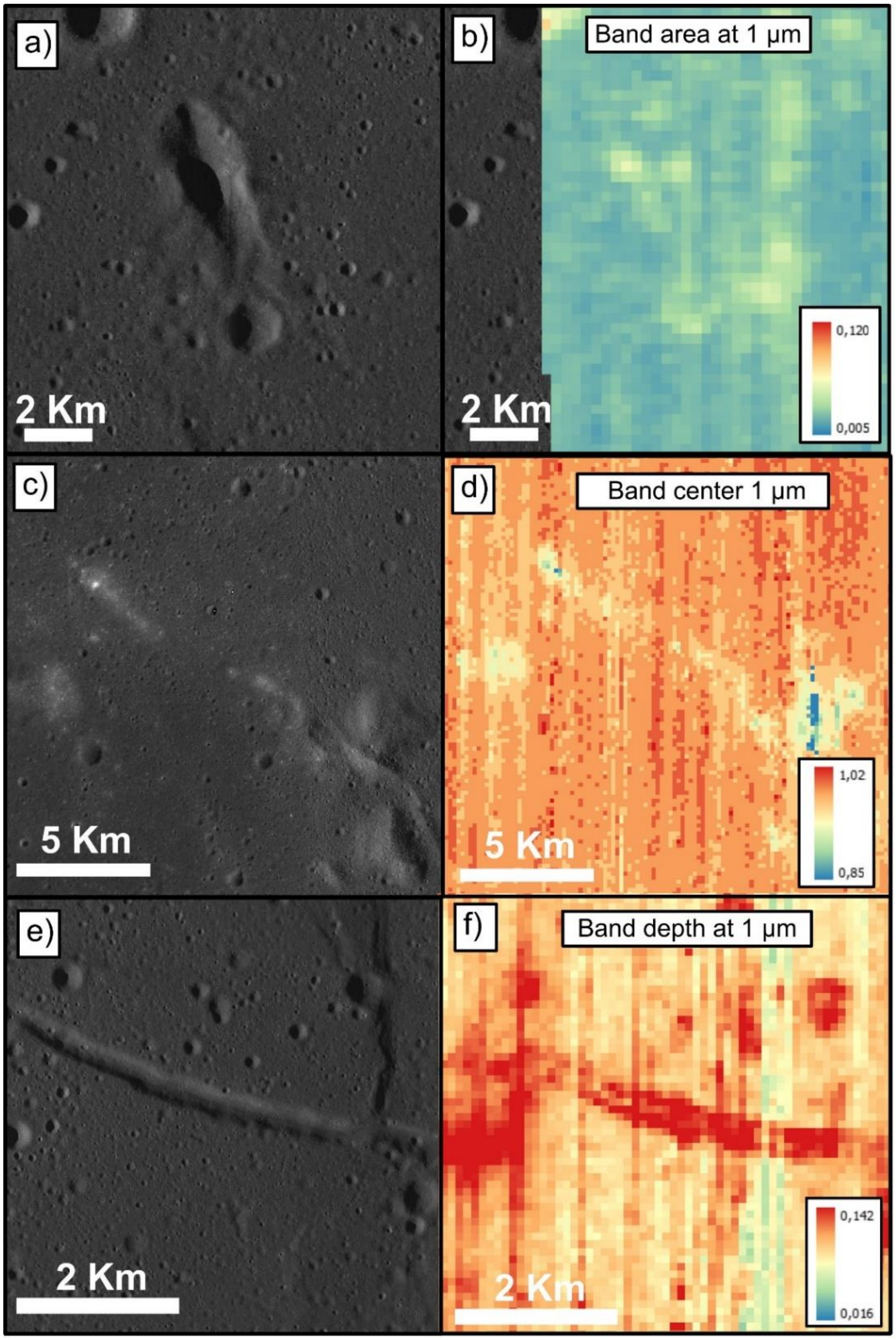

Figure 9: a, b) The volcanic vent does not spectrally differ from the surrounding mare in the band area at 1 μm, which implies that the vent has not erupted in recent times. c, d) The band center at 1 μm of the dyke is lower, which implies there is a

smaller abundance of mafic minerals or a difference in soil maturity. e, f) The walls of the main rille have a strong absorption in the band dept at 1 μm, which implies that the rocks are fresher.

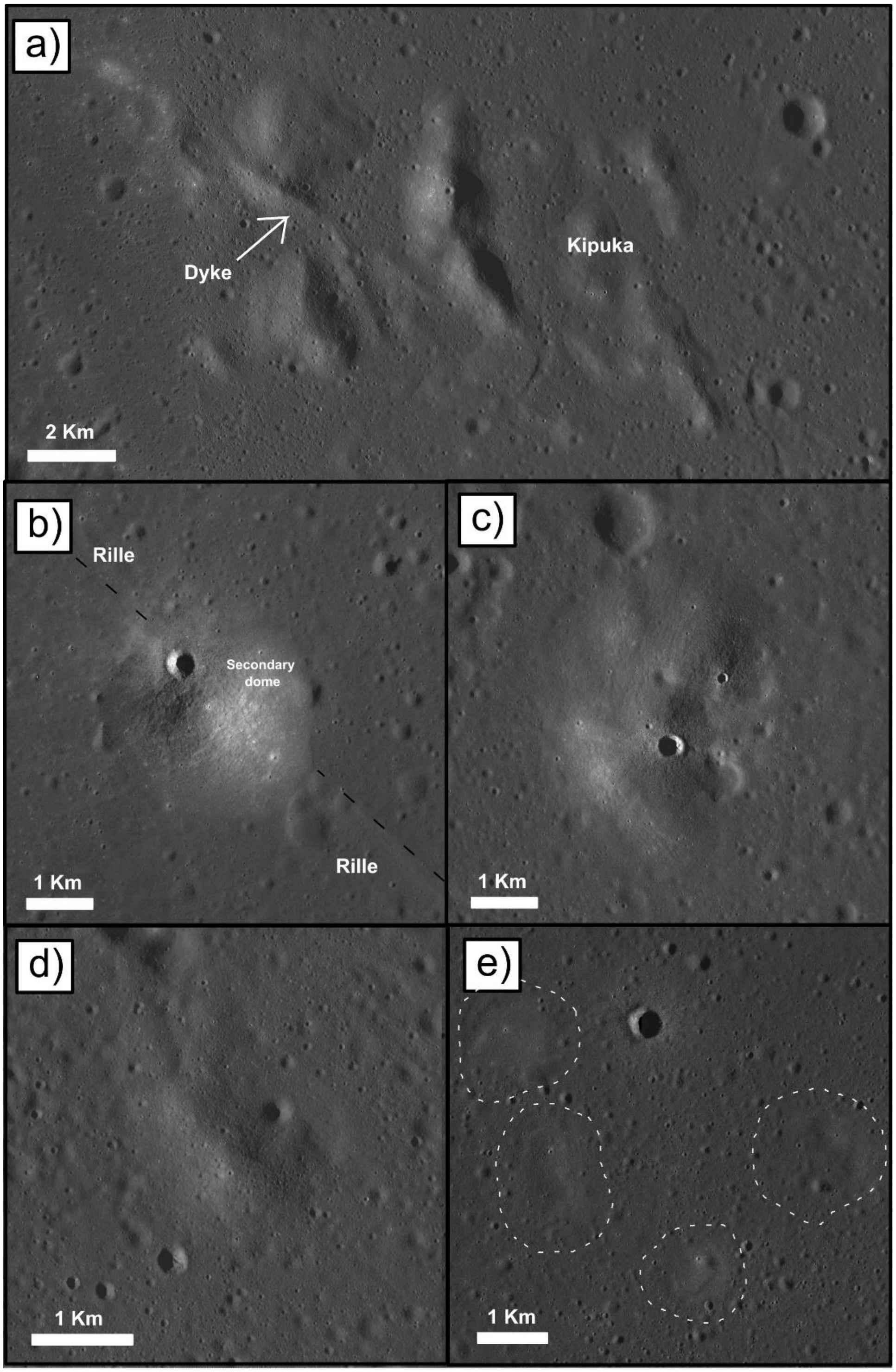

Figure 10: Type of secondary structures inside V1. a) Kipukas, remnants of ancient ejecta embedded in the mare, and a dyke that intruded the west part of the group.

b) Secondary dome *Esd1*, a round and bright structure superimposed to the main rille crossing V1, implying a younger age. c) Secondary dome Esd2, irregularly shaped, it is the biggest of these structures. d) One dome of the Esd3 units, smaller than the previous ones, with a similar tonality to the surrounding mare. e) A group of four domes of the Esd4 unit, they are small hills nearly indistinguishable from their surroundings.

4.3 Structural considerations

The rilles, wrinkle ridges, and grabens that were too small to be represented as units were mapped as linear features (**Figure 7**). Regardless of the size, local wrinkles ridges have a preferential NE-SW trend, which is aligned with the regional pattern of bigger structures. The area around V1 is heavily fractured due to a network of rilles and faults that developed on top of it. Two compressional structures were found. The first one is a major thrust fault that limits the eastern flank of V1, creating a scarp that reaches 60 m in height. The most significant uplift occurs toward the middle of the dome, where it is cut by the main rille; while to the north and south, the scarp gradually fades, becoming almost indistinguishable from the mare. The scarp is also displaced horizontally when it meets the main rille, which is caused by a strike-slip fault that developed at this location (**Figure 11**). The second important thrust fault was found to the east of V1, following the end of the main rille, linked to a 15 km long scarp and the structural hills of the unit ***Esh***.

Grabens and rilles are the result of extensional stress, and they dominate the area following two main directional trends. The main rille cuts the dome in an NW-SE direction, similar to the trend of other smaller fractures. The middle section of the main rille is not completely developed (thin section of the rille on top of V1 in **Figure 7**), instead an incipient and long normal fault connects the more developed portions of the rille to the north and south. Another major deformation occurs in an almost perpendicular direction, where two minor rilles run from the southern half of V2 to intercept the main rille, following an NE-SW trend.

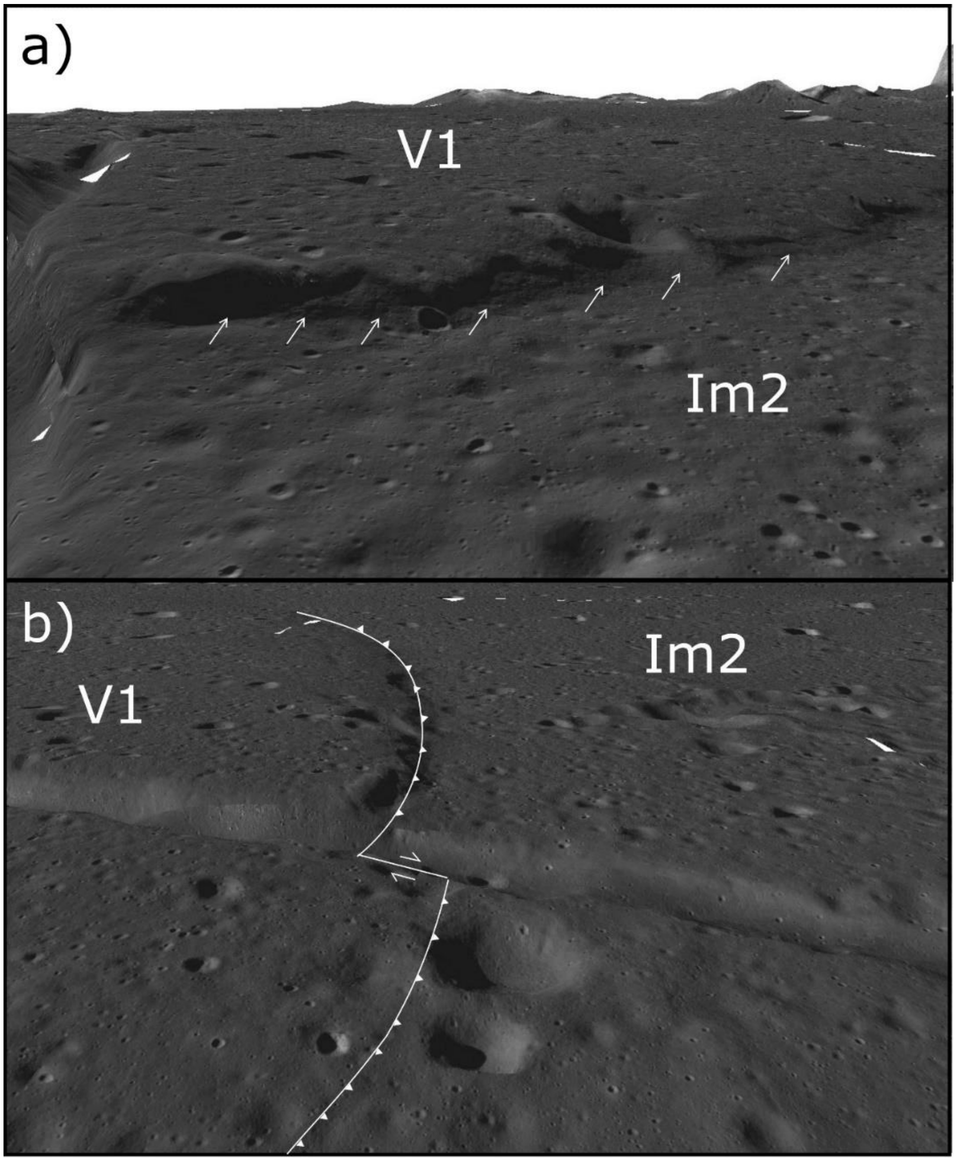

Figure 11: Structural features of V1. a) The east flank of V1 is a scarp up to 60 m high, this section is uplifted by a thrust fault. b) When the mentioned scarp crosses the main linear rille, the feature is translated by a dextral strike-slip fault. South of the rille the scarp is still visible, but it is smaller.

4.4 Crater size-frequency distribution

It was difficult to establish the relative age of the domes since the material covering the intrusions corresponds to the flood basalts that fill the basin, making a standard crater counting technique not viable since it would only retrieve the age of the latest lava flow event. Nevertheless, an alternative method known as buffer crater counting can be applied to linear features (Tanaka 1982, Fassett and Head, 2008), and the rilles cutting V1 and V2 are long enough to conduct this analysis. The method consists of counting the craters that intersect the linear feature in question; given that this produces too few data points, we also counted the craters whose ejecta also overlap the linear features. The total area of the intersecting craters was buffered around the linear feature, and the age was computed using the software CraterStats (Michael 2021; Kneissl et al. 2015). We also applied the usual crater counting technique to the flood lavas on top of both domes. The mapped areas and the resulting ages can be seen in **Figure 12**.

We estimated ages of 2.59 ± 0.3 Ga and 3.32 ± 0.1 Ga for the units ***Em1*** and ***Im2,*** respectively (both mantling V1) (**Figure 12b, 12c**), while for the unit ***Im3*** (mantling V3), we calculated an age of 3.66 ± 0.01 Ga (**Figure 12d**). These estimations disagree with those of Hiesinger et al. (2011), probably due to the far smaller area comprised in our analysis. Still, the stratigraphic relationships between the units remain the same, the materials on top of V3 (***Im3***) are older than those over V1 (***Im1*** and ***Im2***). Although these ages do not correspond to the intrusion of the domes, they put an upper limit on their formation. The lower limit is given by the ages of the buffered crater counting, which gives 1.88 ± 0.5 Ga and 2.06 ± 0.4 Ga for the two parts of the main rille cutting V1, and 1.81± 0.3 Ga for the small rille on V3.

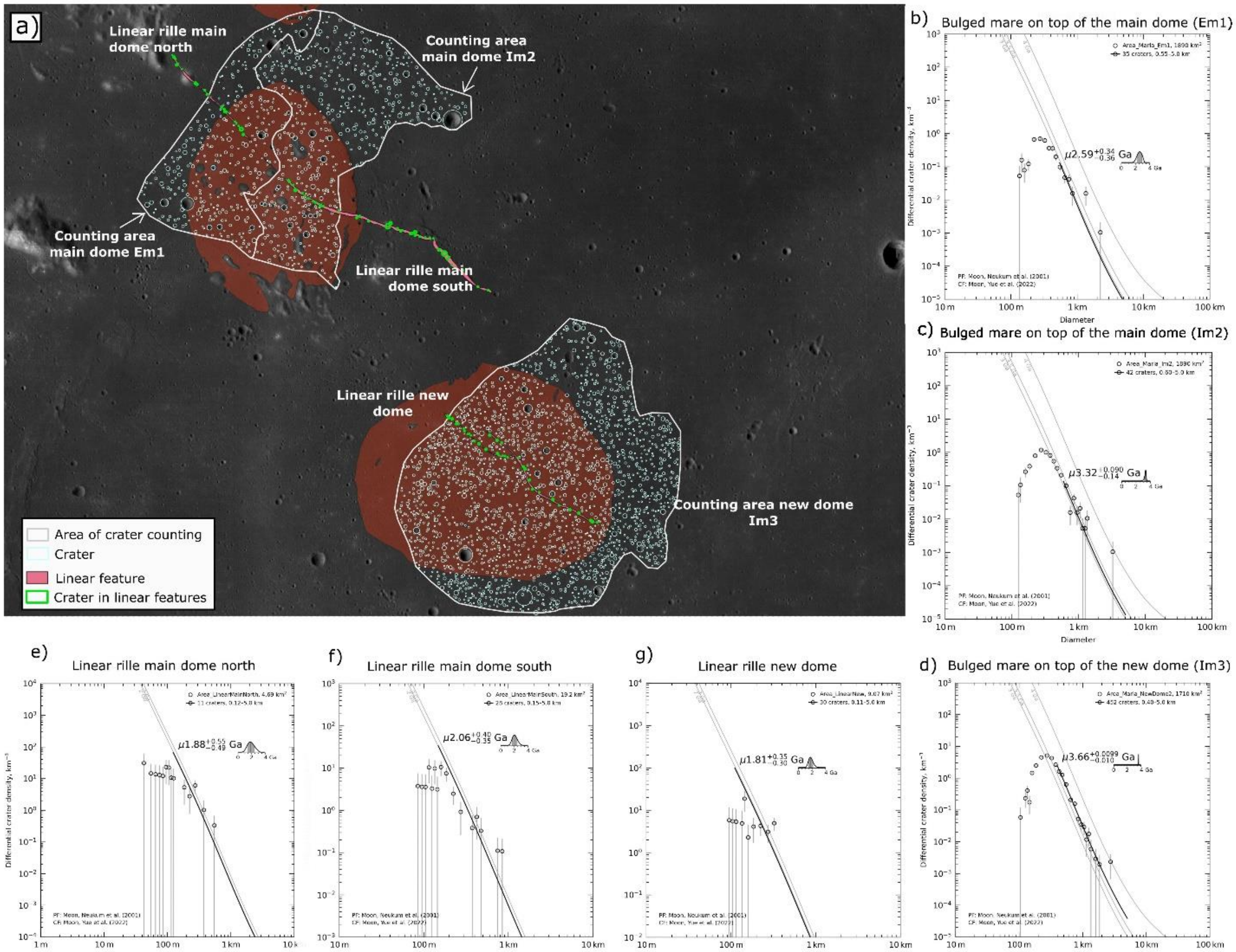

Figure 12: Crater counting analysis. a) The two areas where the standard crater counting was carried out are shown in white and the craters counted inside in light blue; the analyzed linear features are pink, and the craters that cut them are green. b) and c) the ages of the mare on top of V1 and V2. d), e), f) the age of the linear features using the buffered crater counting method.

5 Discussion

5.1 Kipukas vs Secondary Domes

The origin of the secondary structures on top and around V1 has major implications for the geological history of the area. If they were kipukas, as suggested by Whöler et al. (2009), then the igneous rocks of the intrusive system never reached the surface, contrary to the scenario of them being secondary domes. The criteria to differentiate them were both geomorphological and spectral. The shape of the structures can be classified between irregular and oval-shaped. The irregular ones have a sharp contact with the mare units, and internally they consist of scattered hills. Their texture resembles the rim units, and if they originated as ejecta, it would be consistent with their lack of orientation (**Figure 10a**). The oval-shaped structures are round and dome-like, have diffused contacts with the mare units, and have an average height of 100 m, which is lower than the irregular-shaped structures (~250 m) (**Figure 10b, 10c, 10d, 10e**). Some are aligned along two preferential directions, while the non-aligned ones lie on top or near the main rille. These properties, and their clustering near V1, suggest that the oval-shaped structures originated from an igneous process. The lack of pyroclasts and craters on their summits indicates they are not cinder cones, as would be the case for structures in other lunar locations (Henderson et al., 2023).

A spectral analysis was useful to further discriminate between these structures (**Figure 13**). We produced an RGB composite where the red channel represents the spectral slope at 1 µm, the green channel the band center at 1 µm, and the blue channel the band depth at 2 µm (**Figure 13a**). This representation highlights the differences between the types of secondary structures, as both the kipukas (***Ik***) and the rim unis (***Ihim)*** are represented by the same orange color, while the secondary intrusive domes are seen in various tonalities of pink. Furthermore, color differences are noticeable between the secondary domes. A dome directly associated with the linear rille appears in bright pink (***Esd1***), the larger dome in the area has a red-yellow tone (***Esd2***), a set of domes aligned with a NE-SW trend are pale pink (***Esd3***), and the final group is aligned in an NW-SE trend and has a pink-yellow color (***Esd4***).

We also compared the spectral signatures of every type of secondary structure, as well as the background mare (***Im2***). The spectra were analyzed after removing the continuum from the signal (**Figure 13b**). The weaker absorptions are found in the ***Ik*** and ***Ihim*** units, indicating a lower abundance of mafic minerals, and further suggesting the same genesis for both units. The unit ***Im2*** shows strong absorptions at 1 µm and 2 µm, typical of pyroxene-rich basalts. All the spectra of the domes lie between those two types of signatures, suggesting intermediate abundances of mafic minerals. Also, the band center of the signatures from domes is located at shorter wavelengths than those of the ***Im2*** unit, which suggests a higher concentration of Mg-rich pyroxenes (Klima et al., 2011). The units ***Esd1*** and ***Esd2***, especially the latter, have intermediate absorption at 1 µm and a strong absorption at 2 µm, this anomaly is prob.ably related to the presence of spinel, which has a strong absorption around 2 µm, enhancing the typical absorption of pyroxenes (Moriarty et al., 2023). The units ***Esd3*** and ***Esd4*** have a lower reflectance than the other domes near the visible range and at 1.5 µm, suggesting they have a higher maturity than the other domes, and thus may be older (Lucey et al., 2000).

To confirm that our proposed secondary domes are different from the kipukas and the rim units, we conducted a clustering analysis. Since these structures are small at the spatial resolution of M^3, only a few pixels can be sampled for each unit. Therefore, we opted for a direct comparison between the distribution of the band centers of the units, to check if they followed any distinct pattern. We plotted the band center at 1 µm versus the band center at 2 µm for the areas highlighted in **Figure 13a,** each plot contains the scatter of the rim unit ***Ihim*** versus one of the secondary structures (**Figure 13c, 13d, 13e**). Since the band center is strongly related to composition (e.g. Adams, 1974), we would expect a strong clustering of the points if the composition of both units were similar. **Figure 13c** plots the distribution of the units ***Ihim*** and ***Esd3***, although some pixels of both units overlap (black), the majority of the points of ***Ihim*** are clustered at shorter band centers (green), and the ones of ***Esd3*** are concentrated at longer band centers (blue). This indicates that this set of secondary domes is spectrally different from the rim material, further pointing to a difference in their origin. A similar result was found for ***Ihim*** and ***Esd4*** (**Figure 13d**). On the other hand, the same exercise for the ***Ik*** and ***Ihim*** units returned a different result (**Figure 13e**), in this case, the points for both units are scattered with no clear clusters, so the units cannot be spectrally differentiated. From this analysis, we concluded that the ***Ik*** unit is indeed compositionally closer to the rim units, and probably genetically unrelated to other secondary structures.

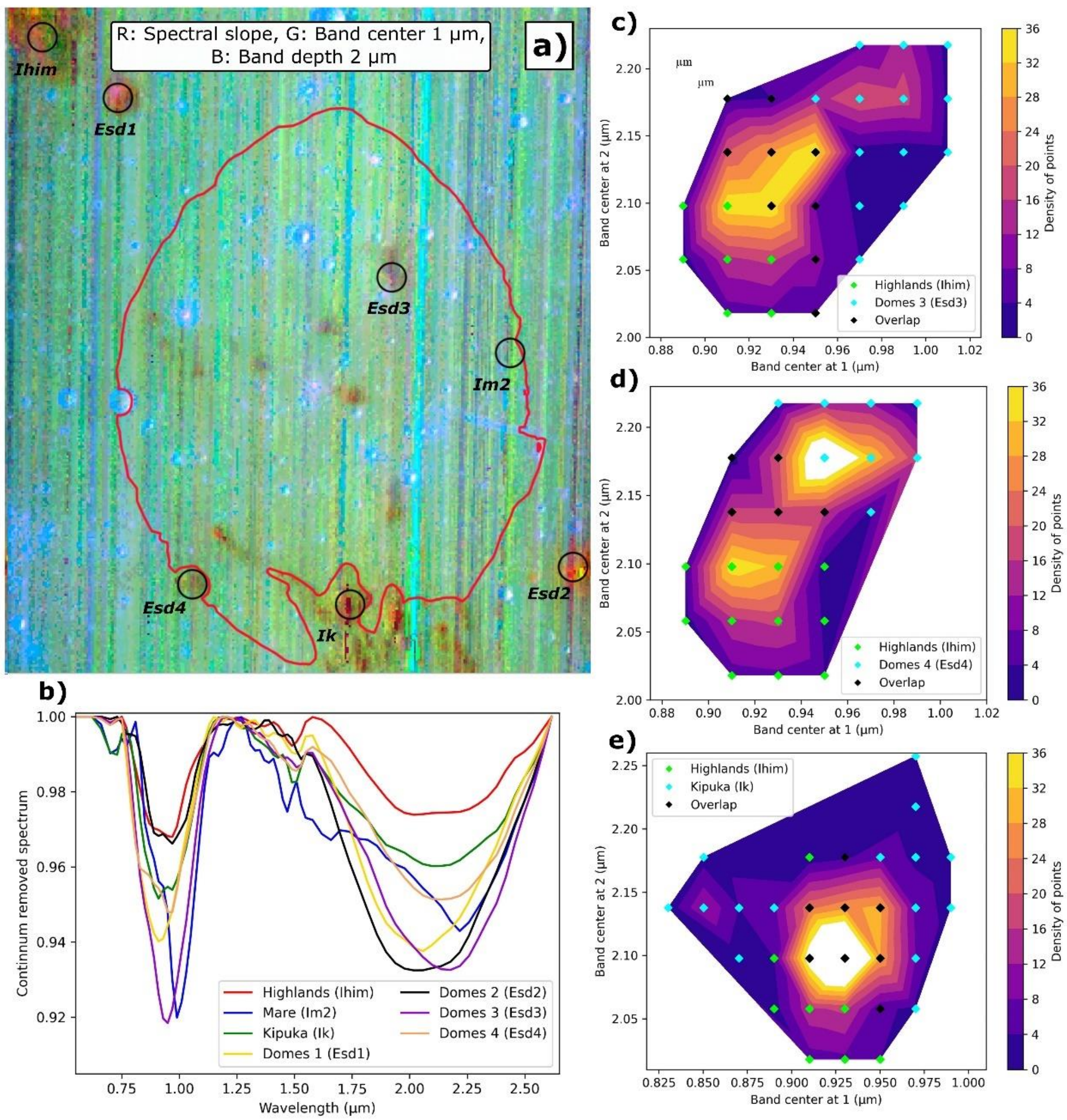

Figure 13: a) RGB composite showing spectral differences between the groups of domes (*Esd1, Esd2, Esd3, Esd4*), kipukas (*Ik*), rim unit (*Ihim*), and mare (*Im2*). b) Plot of the spectra of the different units after the continuum removal, the areas

sampled are highlighted by black circles in Figure 13a. The weaker absorptions are found in the *Ihim* and *Ik* units, while the strongest are in the *Esd2*, *Esd3* and *Im2* units. c) Plot of the band center at 1 µm vs the band center at 2 µm for the pixels inside the black circles in Figure 13a, the contours in the background account for the density of pixels plotted. The plot of the band centers for the *Ihim* and *Esd2* units shows two clear clusters (cyan and green dots), even if there is some overlap between units (black dots). d) The plot of the *Ihim* and *Esd4* units shows a similar result. e) In the case of the *Ihim* and *Ik*, there are no clear clusters of points, so they are not mineralogically distinguishable.

5.2 Geologic evolution

The reconstruction of events in the region had to rely on both the estimation of the formation ages and the stratigraphic relationships between units (**Figure 14**). Given the relatively small geographical scale of some units, such as the secondary domes, the crater-counting approach does not fit the task. Furthermore, some of the domes are concentrated in small areas, so it was not possible to establish clear stratigraphic relationships. In those cases, their formation times were constrained by contextual geological information, as well as the local geological setting.

The first recognizable event was the formation of the Serenitatis Basin. Previous authors tried to associate ages obtained from the radiometric dating of lunar samples to the formation of the basin: Černok et al. (2021) proposed an age of 4.2 Ga, while Spudis et al. (2011) gave a lower limit at 3.8 Ga. Its formation is attributed to the impact of a large asteroid, which created the impact basin, and excavated the ejecta that made up the rim units ***Ihim*** and ***Ihum***, as well as the kipukas (***Ik***) protruding from the mare infill. Another consequence of the impact was the thinning and fracturing of the crust, this weakening subsequently allowed the emplacement of extended flood basalts derived from mantle materials (e.g. Van Dorn, 1969, Geiss and Rossi, 2013). In our study area, this is represented by three flows: first ***Im3***, which was emplaced around 3.66 ± 0.01 Ga, then ***Im2,*** emplaced around 3.32 ± 0.1 Ga, and finally ***Em1***, which was dated at 2.59 ± 0.3 Ga. The formation of wrinkle ridges (***Iwr***) and structural grabens (***Isg***) is related to the thermal evolution of the flood basalts (Watters, 1988), which started as soon as the first lava flow began to cool down and continued until the last pulse reached thermal stability. The pair of volcanic vents found in the region (***Evv***) could have formed as early as the emplacement of the first lava pulse, but they might also be related to the later emplacement of the intrusive domes. The latter scenario seems less likely since the vents do not share spectral or structural properties with the intrusive system.

The emplacement of the large domes ***Ev1***, ***Ev2***, and ***Ev3*** is related to the intrusion of a large igneous complex below the area. The location of the intrusive system near the rim of the basin suggests that the upwelling magma was transported along the large annular faults typically formed at the edges of the lunar impact basins (Collins et al., 2022). The area enclosing the three domes is also slightly elevated compared to their surroundings, this uplift cross flood basalts of different ages, thus, it likely originated from the underlying intrusive system. The domes have an asymmetric shape, low topography, and sometimes faulted scarps, which are typical properties of laccoliths (Schofield et al., 2021). However, these structures prove difficult to date since a crater-counting approach only produces an AMA of the covering flood lavas. We propose that they formed after all the lava events occurred (after 2.98 Ga), since the three mare units are uplifted by at least one dome. We also know that they predate, or at least formed synchronously with the large rilles (***Er***) on top of V1 and V2. These linear features are the result of intruding dykes stalled near the surface, which were also fed by the larger intrusive body. The rilles are dated between 1.81 ± 0.3 and 2.06 ± 0.4 Ga, which would also be the lower limit to the formation of the laccoliths. At least V1 continued raising after this time, since the main rille is slightly uplifted where it crosses the thrust fault limiting V1 to the east. The secondary domes ***Esd1***, ***Esd2***, ***Esd3***, and ***Esd4*** are small intrusions likely related to intruding dykes. Even if only ***Esd1*** were superimposed to the main rille, the alignment of the other sets of domes points to a similar origin. This means that these later domes formed after 1.88 ± 0.5 Ga. We know that the four groups are mineralogically different, meaning that they formed from different sources of magma and probably at different times. Nevertheless, we could not establish stratigraphic relationships between them to further discriminate their formation sequence. Our mapping suggests that ***Esd1*** and ***Esd2*** are younger, due to their sharp borders and higher reflectance in the visible range.

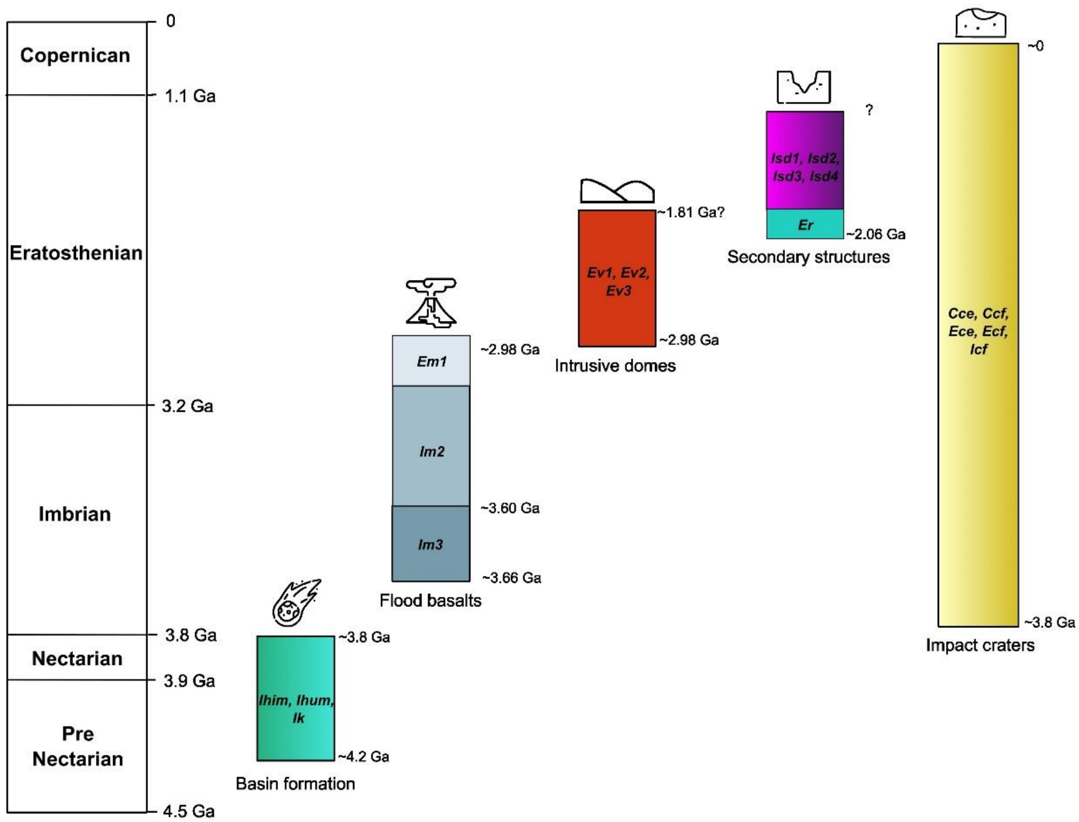

Figure 14: Geological evolution of the area. The Serenitatis basin and its rim were formed by a meteorite impact, this created the rim units and kipukas, and triggered the emplacement of flood lavas. The main domes intruded after the last flood event and the formation of the main rilles, which was followed by the formation of dykes, secondary domes and smaller rilles. Finally, asteroid impacts have occurred throughout time.

5.3 Potential reservoirs

On Earth, intrusive bodies represent important reservoirs of mineral resources. Some minerals are hosted in the intrusive body itself, such as the Platinum Groups Elements (PGE), an example is the Stillwater complex in the United States (Page, 1977; Lightfoot and Evans-Lamswood, 2014). Other resources are generated by the interaction of the intrusion with external factors, such as the formation of skarns in the Yeshan deposit in China, due to contact metamorphism between the intrusion and the host rock (Zhao et al., 2022). There is a potential for the Valentine domes and other secondary domes to host minerals of interest for the upcoming lunar exploration. However, there are some differences between the intrusions on the Earth and those on the Moon. The lunar crust and mantle are at least moderately depleted of water (Hauri et al., 2015), this greatly inhibits the mobilization of minerals hosted in the intrusion to the areas with contact metamorphism and beyond, which is the main mechanism of mineral concentration in these systems. This makes it less likely that skarn-like or hydrothermal-related deposits could have developed on the Moon. Another important difference is that the dominant composition of the lunar rocks is basaltic, as in the case of the Valentine domes, consequently, deposits related to felsic intrusions would not be common, apart from some specific cases like the Gruithuisen domes (e.g. Braden and Robinson, 2011). Given this context, mineralizations in lunar intrusions, if present, would be more like those where the ore minerals are hosted inside the intruding mafic rocks themselves, like the Stillwater complex or the great Zimbabwe dyke (Wilson, 1996). Commonly, valuable materials accumulate in those settings, especially iron, PGE, and chromites. The main dome of the Valentine system has an interesting feature in the thrust fault that defines its eastern flank, intrusive rocks may be outcropping along the hanging block of the thrust, facilitating access to the intruding rocks. Furthermore, the fault itself and the network of fractures associated with it can act as weak areas where minerals can be hosted. Finally, although the data of M^3 is good enough to analyze the general mineralogy of a region, datasets with higher resolution would be necessary to address the real potential of ore minerals in these systems, as well as the recovery of physical samples that could be analyzed in the laboratory.

6 Conclusions

Intrusive domes are probably one of the least studied landforms on the Moon. This is because intrusive processes are hard to observe due to their subtle effects on the surface. We found that given their low topography, large extent, and small slope, the aspect map is a key product to help identify them. This product clearly shows the direction of the slope, indifferently of its magnitude, thus accentuating the physical boundaries of the domes. We are confident that there is still a considerable number of intrusive domes that have not been identified in remote sensing data. A closer observation of high-resolution DEMs and aspect maps may reveal new domes hidden in plain sight, like V3.

Intrusive domes are medium-sized structures that tend to occur in clusters, making the use of low-resolution data to study them limiting. Some datasets like the gravitational anomaly map derived from GRAIL are too coarse to retrieve meaningful information, but products with a medium resolution like M^3 can be useful. Even if a spectral analysis of an intrusive dome will mainly return information on the covering units, some information can be derived from secondary structures. In the case of the Valentine system, the secondary structures were too small to use the spectral data of M^3 as the primary means of classification. Nevertheless, with the aid of previously defined geomorphological units, it was possible to spot and contextualize clear differences between units using spectral indexes and clustering spectral parameters.

The intrusive system beneath the Valentine dome is bigger than previously estimated, the newly discovered dome V3 is the biggest in the system, and together with V1, they are part of a larger uplifted region. Some of the secondary structures on top of V1 are morphologically and compositionally different from the rim units, suggesting they are not kipukas; they are also aligned with each other and with the main rille on V1, which we propose was formed by a dyke stalled near the surface. Even though the compositional information about the secondary domes is not conclusive, we believe there is enough evidence to consider them as also igneous in origin. These structures record the history of an intrusive system that was active for several million years, after 2.98 ± 0.15 Ga and at least until 1.88 ± 0.5 Ga ago. The number of secondary domes, fault systems, and dyke networks interacting within the Valentine domes makes this location one of the most intriguing intrusive systems on the Moon, and thus an attractive target for future exploration.

Acknowledgments

We thank the reviewers for their detailed comments and suggestions, it helped us to greatly improve the manuscript. This research was carried out within the framework of the EXPLORE project, which received funding from the European Union's 2020 research and innovation program under grant agreement No 101004214. Additionally, we had support from the GMAP project, part of the Europlanet 2024 RI that has received funding from the European Union's Horizon 2020 research and innovation programme under grant agreement No 871149.

Open Research

The raw datasets used in this work (NAC and M^3), can be accessed through the PDS (Robinson, 2009; Malaret, 2011). The ***MoonIndex*** software is available for Python 3.10 and higher in the PyPI repository. The source code, exemplary Jupyter notebooks, definition of functions, and workflows can be accessed via GitHub and Zenodo (Suárez-Valencia, 2024). The processed geospatial dataset, QGIS project, and final maps can also be accessed via Zenodo (Suárez-Valencia and Rossi, 2024).

References

Adams, J. B. (1974). Visible and near-infrared diffuse reflectance spectra of pyroxenes as applied to remote sensing of solid objects in the solar system. Journal of Geophysical Research, 79(32), 4829-4836. https://doi.org/10.1029/JB079i032p04829

Agarwal, N., Haridas, A., Khanna, N., Srivastava, P., & Jain, V. (2019). Study of morphology and degradation of lunar craters using Chandrayaan–1 data. Planetary and Space Science, 167, 42-53. https://doi.org/10.1016/j.pss.2019.01.003

Aileen Yingst, R., Mest, S. C., Brent Garry, W., Williams, D. A., Berman, D. C., & Gregg, T. K. P. (2023). A Geologic Map of Vesta Produced Using a Hybrid Method for Incorporating Spectroscopic and Morphologic Data. The Planetary Science Journal, 4(9), 157. https://doi.org/10.3847/PSJ/acebe9

Azzaro, Raffaele. (2012). The volcano-tectonic map of Etna volcano, 1:100.000 scale: An integrated approach based on a morphotectonic analysis from high-resolution

DEM constrained by geologic, active faulting and seismotectonic data. Italian Journal of Geosciences, Vol. 131, n. 1, 153-170. https://doi.org/10.3301/IJG.2011.29

Barker, M. K., Mazarico, E., Neumann, G. A., Zuber, M. T., Haruyama, J., & Smith, D. E. (2016). A new lunar digital elevation model from the Lunar Orbiter Laser Altimeter and SELENE Terrain Camera. Icarus, 273, 346-355. https://doi.org/10.1016/j.icarus.2015.07.039

Beyer, R. A., Alexandrov, O., & McMichael, S. (2018). The Ames Stereo Pipeline: NASA's Open Source Software for Deriving and Processing Terrain Data. Earth and Space Science, 5(9), 537-548. https://doi.org/10.1029/2018EA000409

Braden, S. E., & Robinson, M. S. (2011). Human exploration of the Gruithuisen Domes. En W. B. Garry & J. E. Bleacher, Analogs for Planetary Exploration. Geological Society of America. https://doi.org/10.1130/2011.2483(30)

Bretzfelder, J. M., Klima, R. L., Greenhagen, B. T., Buczkowski, D. L., Petro, N. E., & Day, M. (2020). Identification of Potential Mantle Rocks Around the Lunar Imbrium Basin. Geophysical Research Letters, 47(22). https://doi.org/10.1029/2020GL090334

Cahill, J. T. S., Lucey, P. G., & Wieczorek, M. A. (2009). Compositional variations of the lunar crust: Results from radiative transfer modeling of central peak spectra. Journal of Geophysical Research: Planets, 114(E9), 2008JE003282. https://doi.org/10.1029/2008JE003282

Canale, M., Wright, J., & Rothery, D. A. (2024). A hybrid geological map of Sibelius Crater on Mercury, and its associated ejecta and impact melt deposits. Geological Society, London, Special Publications, 541(1), SP541-2022-2296. https://doi.org/10.1144/SP541-2022-296

Černok, A., White, L. F., Anand, M., Tait, K. T., Darling, J. R., Whitehouse, M., Miljković, K., Lemelin, M., Reddy, S. M., Fougerouse, D., Rickard, W. D. A., Saxey, D. W., & Ghent, R. (2021). Lunar samples record an impact 4.2 billion years ago that may have formed the Serenitatis Basin. Communications Earth & Environment, 2(1), 120. https://doi.org/10.1038/s43247-021-00181-z

Collins, M. S., Byrne, P. K., Klimczak, C., & Mazarico, E. (2023). Thrust Faults Bound an Elevated Mantle Plug Beneath Several Lunar Basins. Journal of Geophysical Research: Planets, 128(1), e2022JE007682. https://doi.org/10.1029/2022JE007682

Fassett, C. I., & Head, J. W. (2008). The timing of martian valley network activity: Constraints from buffered crater counting. Icarus, 195(1), 61-89. https://doi.org/10.1016/j.icarus.2007.12.009

Florinsky, I. V. (2012). Morphometric Variables. En Digital Terrain Analysis in Soil Science and Geology (pp. 7-30). Elsevier. https://doi.org/10.1016/B978-0-12-385036-2.00002-X

Fortezzo, C. M., Spudis, P. D., & Harel, S. L. (2020). Unified Geologic Map of the Moon [Map]. Astrogeology.

https://astrogeology.usgs.gov/search/map/Moon/Geology/Unified_Geologic_Map_of_the_Moon_GIS_v2

Garfinkle, R. A. (2020). Observing Lunar Rilles, Rupes, and Vallis. En R. A. Garfinkle, Luna Cognita (pp. 941-954). Springer New York. https://doi.org/10.1007/978-1-4939-1664-1_25

Geiss, J., & Rossi, A. P. (2013). On the chronology of lunar origin and evolution: Implications for Earth, Mars and the Solar System as a whole. The Astronomy and Astrophysics Review, 21(1), 68. https://doi.org/10.1007/s00159-013-0068-1

Goossens, S., Fernández Mora, Á., Heijkoop, E., & Sabaka, T. J. (2021). Patched Local Lunar Gravity Solutions Using GRAIL Data. Earth and Space Science, 8(11), e2021EA001695. https://doi.org/10.1029/2021EA001695

Graham, R. L. (1972). An efficient algorith for determining the convex hull of a finite planar set. Information Processing Letters, 1(4), 132-133. https://doi.org/10.1016/0020-0190(72)90045-2

Gustafson, J. O., Bell, J. F., Gaddis, L. R., Hawke, B. R., & Giguere, T. A. (2012). Characterization of previously unidentified lunar pyroclastic deposits using Lunar Reconnaissance Orbiter Camera data. Journal of Geophysical Research: Planets, 117(E12), 2011JE003893. https://doi.org/10.1029/2011JE003893

Hackman, R. J. (1966). Geologic map of the Montes Apenninus region on the Moon [Map]. USGS.

Hartmann, W. K., & Wood, C. A. (1971). Moon: Origin and evolution of multi-ring basins. The Moon, 3(1), 3-78. https://doi.org/10.1007/BF00620390

Hauri, E. H., Saal, A. E., Rutherford, M. J., & Van Orman, J. A. (2015). Water in the Moon's interior: Truth and consequences. Earth and Planetary Science Letters, 409, 252-264. https://doi.org/10.1016/j.epsl.2014.10.053

Head, J. W., & Wilson, L. (2017). Generation, ascent and eruption of magma on the Moon: New insights into source depths, magma supply, intrusions and effusive/explosive eruptions (Part 2: Predicted emplacement processes and observations). Icarus, 283, 176-223. https://doi.org/10.1016/j.icarus.2016.05.031

Henderson, M. J. B., Horgan, B. H. N., Lawrence, S. J., Stopar, J. D., & Gaddis, L. R. (2023). Mineralogy of explosive and effusive volcanic edifices in the Marius Hills Volcanic Complex. Icarus, 404, 115628. https://doi.org/10.1016/j.icarus.2023.115628

Hiesinger, H., Head, J. W., Wolf, U., Jaumann, R., & Neukum, G. (2011). Ages and stratigraphy of lunar mare basalts: A synthesis. En W. A. Ambrose & D. A. Williams, Recent Advances and Current Research Issues in Lunar Stratigraphy. Geological Society of America. https://doi.org/10.1130/2011.2477(01)

Horgan, B. H. N., Cloutis, E. A., Mann, P., & Bell, J. F. (2014). Near-infrared spectra of ferrous mineral mixtures and methods for their identification in planetary surface spectra. Icarus, 234, 132-154. https://doi.org/10.1016/j.icarus.2014.02.031

Hutton, D. H. W. (1988). Granite emplacement mechanisms and tectonic controls: Inferences from deformation studies. Earth and Environmental Science Transactions of the Royal Society of Edinburgh, 79(2-3), 245-255. https://doi.org/10.1017/S0263593300014255

Huang, J., Xiao, L., He, X., Qiao, L., Zhao, J., & Li, H. (2011). Geological characteristics and model ages of Marius Hills on the Moon. *Journal of Earth Science*, *22*(5), 601-609. https://doi.org/10.1007/s12583-011-0211-8

Kerr, A. D., & Pollard, D. D. (1998). Toward more realistic formulations for the analysis of laccoliths. Journal of Structural Geology, 20(12), 1783-1793. https://doi.org/10.1016/S0191-8141(98)00071-6

Klima, R. L., Pieters, C. M., Boardman, J. W., Green, R. O., Head, J. W., Isaacson, P. J., Mustard, J. F., Nettles, J. W., Petro, N. E., Staid, M. I., Sunshine, J. M., Taylor, L. A., & Tompkins, S. (2011). New insights into lunar petrology: Distribution and composition of prominent low-Ca pyroxene exposures as observed by the Moon Mineralogy Mapper (M 3). Journal of Geophysical Research, 116, E00G06. https://doi.org/10.1029/2010JE003719

Kneissl, T., Michael, G. G., Platz, T., & Walter, S. H. G. (2015). Age determination of linear surface features using the Buffered Crater Counting approach – Case studies of the Sirenum and Fortuna Fossae graben systems on Mars. Icarus, 250, 384-394. https://doi.org/10.1016/j.icarus.2014.12.008

Kneissl, T., Van Gasselt, S., & Neukum, G. (2011). Map-projection-independent crater size-frequency determination in GIS environments—New software tool for ArcGIS. Planetary and Space Science, 59(11-12), 1243-1254. https://doi.org/10.1016/j.pss.2010.03.015

Laura, J., Acosta, A., Addair, T., Adoram-Kershner, L., Alexander, J., Alexandrov, O., Alley, S., Anderson, D., Anderson, J., Anderson, J., Annex, A., Archinal, B., Austin, C., Backer, J., Barrett, J., Bauck, K., Bauers, J., Becker, K., Becker, T., … Young, A. (2023). Integrated Software for Imagers and Spectrometers (7.2.0_RC1) [Software]. Zenodo. https://doi.org/10.5281/ZENODO.2563341

Lena, R., Wöhler, C., Phillips, J., & Chiocchetta, M. T. (2013). Lunar Domes. Springer Milan. https://doi.org/10.1007/978-88-470-2637-7

Robinson, M., (2009). [dataset]. LRO MOON LROC 2 EDR V1.0. NASA Planetary Data System. https://doi.org/10.17189/1520250

Laul, J. C., & Schmitt, E. A. (1973). Chemical composition of Luna 20 rocks and soil and Apollo 16 soils. *Geochimica et Cosmochimica Acta*, *37*(4), 927-942. https://doi.org/10.1016/0016-7037(73)90190-7

Lightfoot, P. C., & Evans-Lamswood, D. (2015). Structural controls on the primary distribution of mafic–ultramafic intrusions containing Ni–Cu–Co–(PGE) sulfide mineralization in the roots of large igneous provinces. Ore Geology Reviews, 64, 354-386. https://doi.org/10.1016/j.oregeorev.2014.07.010

Liu, T., Michael, G., Zuschneid, W., Wünnemann, K., & Oberst, J. (2021). Lunar megaregolith mixing by impacts: Evaluation of the non-mare component of mare soils. Icarus, 358, 114206. https://doi.org/10.1016/j.icarus.2020.114206

Lucey, P. G., Blewett, D. T., Taylor, G. J., & Hawke, B. R. (2000). Imaging of lunar surface maturity. Journal of Geophysical Research: Planets, 105(E8), 20377-20386. https://doi.org/10.1029/1999JE001110

Lucey, P. G., Greenhagen, B., Donaldson Hanna, K., Bowles, N., Flom, A., & Paige, D. A. (2021). Christiansen Feature Map From the Lunar Reconnaissance Orbiter Diviner Lunar Radiometer Experiment: Improved Corrections and Derived Mineralogy. Journal of Geophysical Research: Planets, 126(6), e2020JE006777. https://doi.org/10.1029/2020JE006777

Malaret. (2011). CH1-ORB MOON M3 4 L2 REFLECTANCE NEAR-IR SPECTRAL IMGS V1.0 [dataset]. NASA Planetary Data System. https://doi.org/10.17189/1520414

Marco Figuera, R., Pham Huu, B., Rossi, A. P., Minin, M., Flahaut, J., & Halder, A. (2018). Online characterization of planetary surfaces: PlanetServer, an open-source analysis and visualization tool. Planetary and Space Science, 150, 141-156. https://doi.org/10.1016/j.pss.2017.09.007

McCallum, I. S., & Schwartz, J. M. (2001). Lunar Mg suite: Thermobarometry and petrogenesis of parental magmas. Journal of Geophysical Research: Planets, 106(E11), 27969-27983. https://doi.org/10.1029/2000JE001397

Massironi, M., Rossi, A. P., Wright, J., Zambon, F., Poehler, C., Giacomini, L., Carli, C., Ferrari, S., Semenzato, A., Luzzi, E., Pozzobon, R., Tognon, G., Rothery, D. A., Van Der Bogert, C., Galluzi, V., & Altieri, F. (2021). From morpho-stratigraphic to geo(spectro)-stratigraphic units: The PLANMAP contribution. Planetary Geologic Mappers 2021.

McCauley, J. F. (1967). Geologic map of the Hevelius region of the moon. U.S. Geological Survey Report, 491.

Michael, G. G. (2021). CraterStats (2.0) [Python]. GitHub. https://github.com/ggmichael/craterstats#BSD-3-Clause-1-ov-file

Miljković, K., Wieczorek, M. A., Collins, G. S., Solomon, S. C., Smith, D. E., & Zuber, M. T. (2015). Excavation of the lunar mantle by basin-forming impact events on the Moon. Earth and Planetary Science Letters, 409, 243-251. https://doi.org/10.1016/j.epsl.2014.10.041

Moriarty, D. P., Simon, S. B., Shearer, C. K., Haggerty, S. E., Petro, N., & Li, S. (2023). Orbital Characterization of the Composition and Distribution of Spinels Across the Crisium Region: Insight From Luna 20 Samples. Journal of Geophysical Research: Planets, 128(5), e2022JE007482. https://doi.org/10.1029/2022JE007482

Neukum, G., Ivanov, B. A., & Hartmann, W. K. (2001). Cratering Records in the Inner Solar System in Relation to the Lunar Reference System. Space Science Reviews, 96(1/4), 55-86. https://doi.org/10.1023/A:1011989004263.

Page, N. J. (1977). Stillwater Complex, Montana: Rock Succesion, Metamoprhisn and Structure of the Complex and Adjacent Rocks (Professional Paper) [Professional Paper].

Papike, J. J., Ryder, G., & Shearer, C. K. (1998). Lunar samples. Reviews in Mineralogy and Geochemistry, 36(1), 5-01.

Penasa, L., & Brandt, C. H. (2021). europlanet-gmap/mappy: Latest (latest) [Software]. Zenodo. https://doi.org/10.5281/ZENODO.5233646

Robinson, M. S., Brylow, S. M., Tschimmel, M., Humm, D., Lawrence, S. J., Thomas, P. C., Denevi, B. W., Bowman-Cisneros, E., Zerr, J., Ravine, M. A., Caplinger, M. A., Ghaemi, F. T., Schaffner, J. A., Malin, M. C., Mahanti, P., Bartels, A., Anderson, J., Tran, T. N., Eliason, E. M., … Hiesinger, H. (2010). Lunar Reconnaissance Orbiter Camera (LROC) Instrument Overview. Space Science Reviews, 150(1-4), 81-124. https://doi.org/10.1007/s11214-010-9634-2

Robinson. (2009). LRO MOON LROC 2 EDR V1.0 [dataset]. NASA Planetary Data System. https://doi.org/10.17189/1520250

Rouault, E., Warmerdam, F., Schwehr, K., Kiselev, A., Butler, H., Łoskot, M., Szekeres, T., Tourigny, E., Landa, M., Miara, I., Elliston, B., Chaitanya, K., Plesea, L., Morissette, D., Jolma, A., & Dawson, N. (2023). GDAL (v3.7.1) [Software]. Zenodo. https://doi.org/10.5281/ZENODO.5884351

Schofield, N., Stevenson, C., Mark, N., & Holford, S. (2021). Igneous Intrusions: Sills, Dykes and Plutons. En Encyclopedia of Geology (pp. 313-329). Elsevier. https://doi.org/10.1016/B978-0-08-102908-4.00112-0

Scott, D. H., & Eggleton, R. E. (1973). Geologic map of the Rumker Quadrangle of the Moon. https://doi.org/10.3133/i805

Shearer, C. K. (2006). Thermal and Magmatic Evolution of the Moon. Reviews in Mineralogy and Geochemistry, 60(1), 365-518. https://doi.org/10.2138/rmg.2006.60.4

Shearer, C. K., Elardo, S. M., Petro, N. E., Borg, L. E., & McCubbin, F. M. (2015). Origin of the lunar highlands Mg-suite: An integrated petrology, geochemistry, chronology, and remote sensing perspective. American Mineralogist, 100(1), 294-325. https://doi.org/10.2138/am-2015-4817

Shearer, C., Neal, C. R., Glotch, T. D., Prissel, T. C., Bell, A. S., Fernandes, V. A., Gaddis, L. R., Jolliff, B. L., Laneuville, M., Magna, T., & Simon, J. (2023). 4 Magmatic Evolution II: A New View of Post-Differentiation Magmatism. En C. R. Neal, L. R. Gaddis, B. L. Jolliff, S. J. Lawrence, S. J. Mackwell, C. K. Shearer, & S. N.

Valencia (Eds.), *New View of the Moon 2* (pp. 147-206). De Gruyter. https://doi.org/doi:10.1515/9781501519895-007

Snyder, G. A., Taylor, L. A., & Halliday, A. N. (1995). Chronology and petrogenesis of the lunar highlands alkali suite: Cumulates from KREEP basalt crystallization. Geochimica et Cosmochimica Acta, 59(6), 1185-1203. https://doi.org/10.1016/0016-7037(95)00034-W

Speyerer, E. J., Robinson, M. S., & Denevi, B. W. (2011). LUNAR RECONNAISSANCE ORBITER CAMERA GLOBAL MORPHOLOGICAL MAP OF THE MOON. 42nd Lunar and Planetary Science Conference.

Spudis, P. D., Wilhelms, D. E., & Robinson, M. S. (2011). The Sculptured Hills of the Taurus Highlands: Implications for the relative age of Serenitatis, basin chronologies and the cratering history of the Moon. Journal of Geophysical Research, 116, E00H03. https://doi.org/10.1029/2011JE003903

Suárez-Valencia, J. E., Rossi, A. P., Zambon, F., Carli, C., & Nodjoumi, G. (2024). MoonIndex , an Open-Source Tool to Generate Spectral Indexes for the Moon From M^3 Data. Earth and Space Science, 11(6), e2023EA003464. https://doi.org/10.1029/2023EA003464

Suárez-Valencia, J. E. (2024). Javierunal16/MoonIndex: Second version of the MoonIndex Python package (2.0.2) [Software]. Zenodo. https://doi.org/10.5281/zenodo.10820503

Suárez-Valencia, J., & Rossi, A. P. (2024). Supporting material for: Geostratigraphic mapping of the intrusive Valentine Domes on the Moon (1.0) [Data set]. Zenodo. https://doi.org/10.5281/zenodo.10849507

Tanaka, K. L. (1982). A new time-saving crater-count technique, with application to narrow features. En NASA Technical Memo, NASA TM-85127 (pp. 123-125). https://ui.adsabs.harvard.edu/abs/1982pggp.rept..123T

Taylor, S. R. (2007). CHAPTER 12—The Moon. En L.-A. McFadden, P. R. Weissman, & T. V. Johnson (Eds.), *Encyclopedia of the Solar System (Second Edition)* (Second Edition, pp. 227-250). Academic Press. https://doi.org/10.1016/B978-012088589-3/50016-5

Tognon, G., Zambon, F., Carli, C., Massironi, M., Giacomini, L., Pozzobon, R., Salari, G., Tosi, F., Combe, J., & Fonte, S. (2024). Integrated Spectral and Compositional

Analysis for the Lunar Tsiolkovskiy Crater. *Journal of Geophysical Research: Planets*, *129*(8), e2023JE008272. https://doi.org/10.1029/2023JE008272

Van Dorn, W. G. (1969). Lunar Maria: Structure and Evolution. Science, 165(3894), 693-695. https://doi.org/10.1126/science.165.3894.693

Wagner, R. V., & Robinson, M. S. (2014). Distribution, formation mechanisms, and significance of lunar pits. Icarus, 237, 52-60. https://doi.org/10.1016/j.icarus.2014.04.002

Watters, T. R. (1988). Wrinkle ridge assemblages on the terrestrial planets. Journal of Geophysical Research: Solid Earth, 93(B9), 10236-10254. https://doi.org/10.1029/JB093iB09p10236

Wieczorek, M. A. (2006). The Constitution and Structure of the Lunar Interior. Reviews in Mineralogy and Geochemistry, 60(1), 221-364. https://doi.org/10.2138/rmg.2006.60.3

Wilson, A. H. (1996). The Great Dyke of Zimbabwe. En Developments in Petrology (Vol. 15, pp. 365-402). Elsevier. https://doi.org/10.1016/S0167-2894(96)80013-3

Wilson, L., & Head, J. W. (2017). Generation, ascent and eruption of magma on the Moon: New insights into source depths, magma supply, intrusions and effusive/explosive eruptions (Part 1: Theory). Icarus, 283, 146-175. https://doi.org/10.1016/j.icarus.2015.12.039

Wöhler, C., & Lena, R. (2009). Lunar intrusive domes: Morphometric analysis and laccolith modelling. Icarus, 204(2), 381-398. https://doi.org/10.1016/j.icarus.2009.07.031

Yue, Z., Di, K., Wan, W., Liu, Z., Gou, S., Liu, B., Peng, M., Wang, Y., Jia, M., Liu, J., & Ouyang, Z. (2022). Author Correction: Updated lunar cratering chronology model with the radiometric age of Chang'e-5 samples. Nature Astronomy, 6(4), 514-514. https://doi.org/10.1038/s41550-022-01649-4

Zhang, F., Head, J. W., Basilevsky, A. T., Bugiolacchi, R., Komatsu, G., Wilson, L., Fa, W., & Zhu, M. (2017). Newly Discovered Ring-Moat Dome Structures in the Lunar Maria: Possible Origins and Implications. *Geophysical Research Letters*, *44*(18), 9216-9224. https://doi.org/10.1002/2017GL074416

Zhang, H., Zhang, X., Zhang, G., Dong, K., Deng, X., Gao, X., Yang, Y., Xiao, Y., Bai, X., Liang, K., Liu, Y., Ma, W., Zhao, S., Zhang, C., Zhang, X., Song, J., Yao, W., Chen, H., Wang, W., … Yang, M. (2021). Size, morphology, and composition of lunar samples returned by Chang'E-5 mission. *Science China Physics, Mechanics & Astronomy*, *65*(2), 229511. https://doi.org/10.1007/s11433-021-1818-1

Zhao, S., Brzozowski, M. J., Mueller, T., Wang, L., & Li, W. (2022). Skarn classification and element mobility in the Yeshan Iron Deposit, Eastern China: Insight from lithogeochemistry. Ore Geology Reviews, 145, 104909. https://doi.org/10.1016/j.oregeorev.2022.104909

Supporting Information for

Geostratigraphic mapping of the intrusive Valentine Domes on the Moon

Javier Eduardo Suarez-Valencia[1], Angelo Pio Rossi[2]

[1]Constructor University Bremen
[2]Earthgraph

Contents of this file

Table S1
Text S1
Figure S1 to S4

Introduction

In this supplementary information we first present a table with all the data used to make the geomorphological maps. Next, we showcase the commands used in ISIS to process the RAW data to create interpretation-ready products. The first two supplementary figures illustrate minor analysis and discussions presented in the main text, while the last two are the full-size maps of the Valentine domes.

Table S1.

Name	Instrument/Mission	Data type
WAC_Mosaic (Speyerer et al., 2011)	WAC, LRO	Image
Bouger_Anomaly (Goossens et al., 2021)	GRAIL	Gravimetry
LRO_Kaguya_DEM (Barket et al., 2016)	Kaguya-LRO	DEM
Global_Plagioclase_Map (Lucey et al., 2021)	DIVINER, LRO	Radar
M3G20090204T233457	M^3, Chandrayaan-1	Hyperspectral
M3G20090205T013151	M^3, Chandrayaan-1	Hyperspectral
M1096429144le	NAC, LRO	Image
M1096429144re	NAC, LRO	Image
M1138844838le	NAC, LRO	Image
M1142369182LE	NAC, LRO	Image
M1142369182RE	NAC, LRO	Image
M1142376293LE	NAC, LRO	Image
M1142376293RE	NAC, LRO	Image
M1142383403LE	NAC, LRO	Image
M1142383403RE	NAC, LRO	Image
M1215373653le	NAC, LRO	Image
M1215373653re	NAC, LRO	Image
M1245960358le	NAC, LRO	Image
M1245960358re	NAC, LRO	Image

M1249458276le	NAC, LRO	Image
M1249458276re	NAC, LRO	Image
M1258875804le	NAC, LRO	Image
M1258875804re	NAC, LRO	Image
M1289445702le	NAC, LRO	Image
M1289445702re	NAC, LRO	Image
M1323551881re	NAC, LRO	Image
M1335299652le	NAC, LRO	Image
M181095207le	NAC, LRO	Image
M181095207re	NAC, LRO	Image

Table listing the data used to perform the mapping.

Table S2.

Index Name	Interpretation
R540	High values (Higher than 0.03) → bright fresh material, plagioclase. Low values (Lower than 0.03) → dark terrain, pyroxene, and other mafic minerals.
BCI	Compositional variations of the principal mineralogical phases (pyroxenes, olivines, and plagioclases). Low-Ca pyroxenes have values lower than 0.99, high-Ca pyroxenes have values higher than 0.99.
BCII	If the band center is shifted to lower wavelengths, it may show abundance of low-Ca pyroxene. Low-Ca pyroxenes have values lower than 2.15, high-Ca pyroxenes have values higher than 2.15.
BDI	Abundance of the principal mineralogical phases and their grain sizes, also abundance of opaque phases. Values depend on the minerals involved and their proportions.
BDII	Abundance of the principal mineralogical phases and their grain sizes, also abundance of opaque phases. Values depend on the minerals involved and their proportions.
SS	Low values → fresh terrains, dark terrain. High values → older terrains, space weathering.
Clem RED	High values imply low titanium regions, or high glass contents.
Clem GREEN	High values show enrichment of iron in the surface, and mafic minerals.
Clem BLUE	Higher values imply high titanium content and bright slopes.

BD1900	Highlights differences in mafic compositions when combined with IBDI and IBDII.
IBDI	It shows high values when olivine and pyroxene are present. Values depend on the minerals involved and their proportions.
IBDII	It shows high values when pyroxene is present. Values depend on the minerals involved and their proportions.
BAI	Useful to differentiate between mineral species. Bigger areas imply the presence of more mafic minerals. When plotted against the band center gives information about the mixture of mafic minerals.
BAII	Useful to differentiate between mineral species. Bigger areas imply the presence of more mafic minerals. When plotted against the band center gives information about the mixture of mafic minerals.
ASYI	Useful to identify glass-bearing mixtures with high asymmetries. Asymmetries higher than 15 points to the presence of glass. When plotted against the band center gives information about the mixture of mafic minerals.
ASYII	Useful to identify glass-bearing mixtures with high asymmetries. When plotted against the band center gives information about the mixture of mafic minerals.
Ol	A higher value implies a major abundance of olivine. This index is only indicative, to properly quantify the amounts of olivine, the use of a radiative transfer model is suggested.
Sp1	A higher value implies a major abundance of spinel. This index is only indicative, it is not intended to be a quantitative tool.
Sp2	A higher value implies a major abundance of spinel. This index is only indicative, it is not intended to be a quantitative tool.
Px	A higher value implies a major abundance of pyroxene. This index is only indicative, it is not intended to be a quantitative tool.
An	A higher value implies a major abundance of anorthosite. This index is only indicative, is it not intended to be a quantitative tool.
BD950	While combined with other indexes to create the RGB6 composite is useful to study lunar maria. A higher value implies the presence of mafic minerals.
BD1050	While combined with other indexes to create the RGB6 composite is useful to study lunar maria. A higher value implies the presence of mafic minerals.

BD1250	While combined with other indexes to create the RGB6 composite is useful to study lunar maria. A higher value implies the presence of mafic minerals.
R1580	While combined with other indexes to create the RGB7 composite is useful to study lunar maria.
Fe	Higher values imply the presence of iron. The percentage of FeO in weight can be derived from the parameter: $wt\%FeO = 8.878 * Fe^{1.8732}$
Ti	Higher values imply the presence of titanium. The percentage of FeO in weight can be derived from the parameter: $wt\%FeO = 2.6275 * Ti^{4.2964}$
Cr	Higher values imply the presence of chromite. This index is only indicative, it is not intended to be a quantitative tool.

Table listing the spectral indexes used to perform the mapping.

Text S1.

The processing of planetary data requires the use of the ISIS and GDAL software, which was done using the following commands:

Listing all files to do the batch processing

```
ls *.IMG | sed s/.IMG// > Imputs.lis
```

Transformation from IMG to cubes

```
lronac2isis from=\$1.IMG to=\$1.cub -batchlist=Imputs.lis
```

Actualization of cubes kernels

```
spiceinit from=\$1.cub -batchlist=Imputs.lis
```

Calibrating for I/F

```
lronaccal from=\$1.cub to=\$1_lv1.cub -batchlist=Imputs.lis
```

NAC instrumental correction

```
lronacecho from=\$1_lv1.cub to=\$1_lv1echo.cub -batchlist=Imputs.lis
```

Map projection, a map template needs to be previously created

```
cam2map from=\$1_lv1echo.cub map=Equirectangular.map to=\$1_lv2.cub
PIXRES=map -batchlist=Imputs.lis
```

Mosaic

```
noseam from=List2.txt to=Final.cub samples=333 lines=333
```

Translate

```
gdal_translate Final.cub Final.tif
```

After these steps, the data is ready for interpretation in a geoprocessing software.

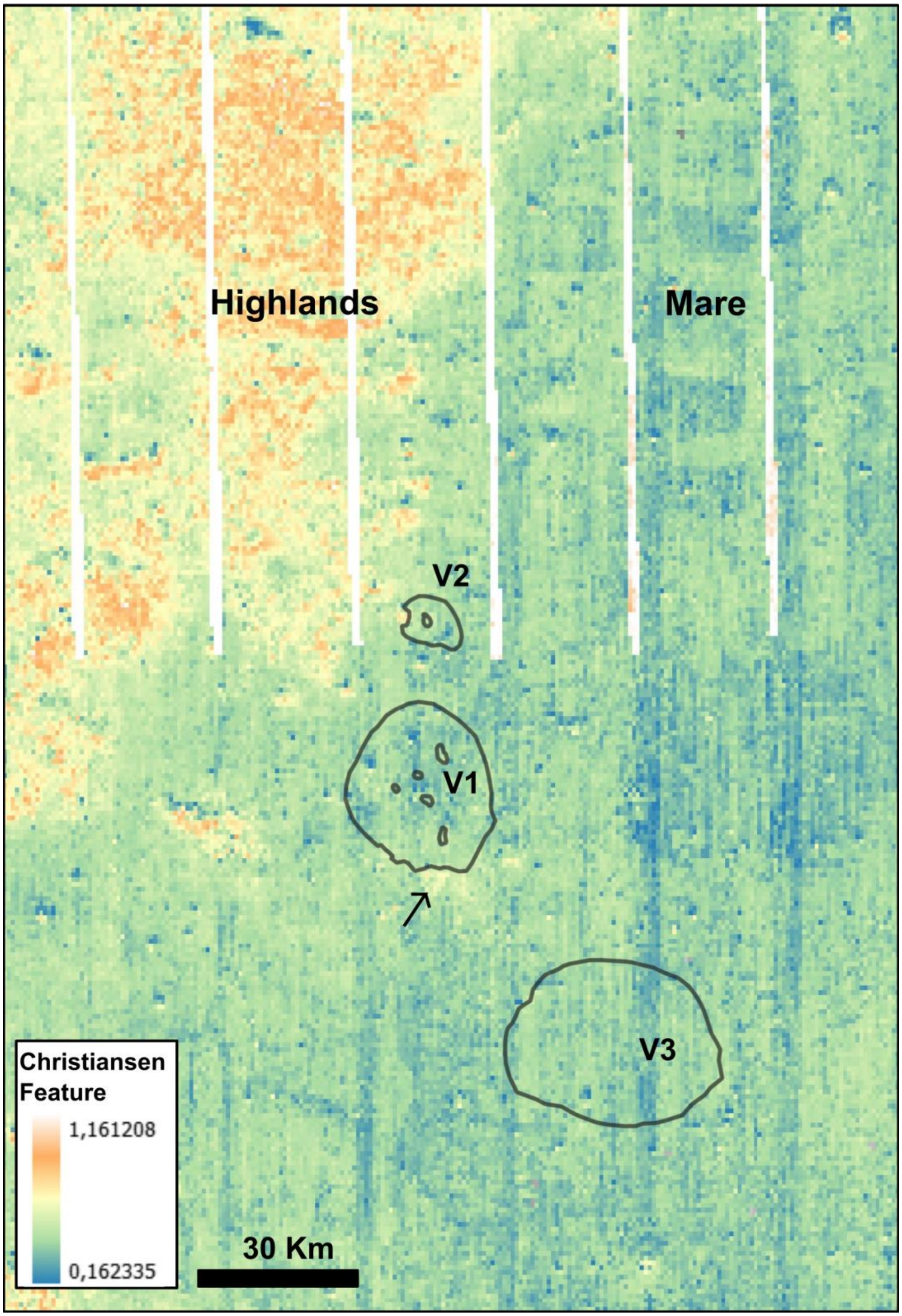

Figure S1. Map of the Christiansen feature of the zone, values increase with the abundance of plagioclase. Higher values are found in the rim of the basin, and lower on the mare and the domes, which is consistent whit the basaltic composition of the mare. A region with intermediate values is found south of V1, which corresponds with the Kipukas (***Ik***) identified in this study (arrow).

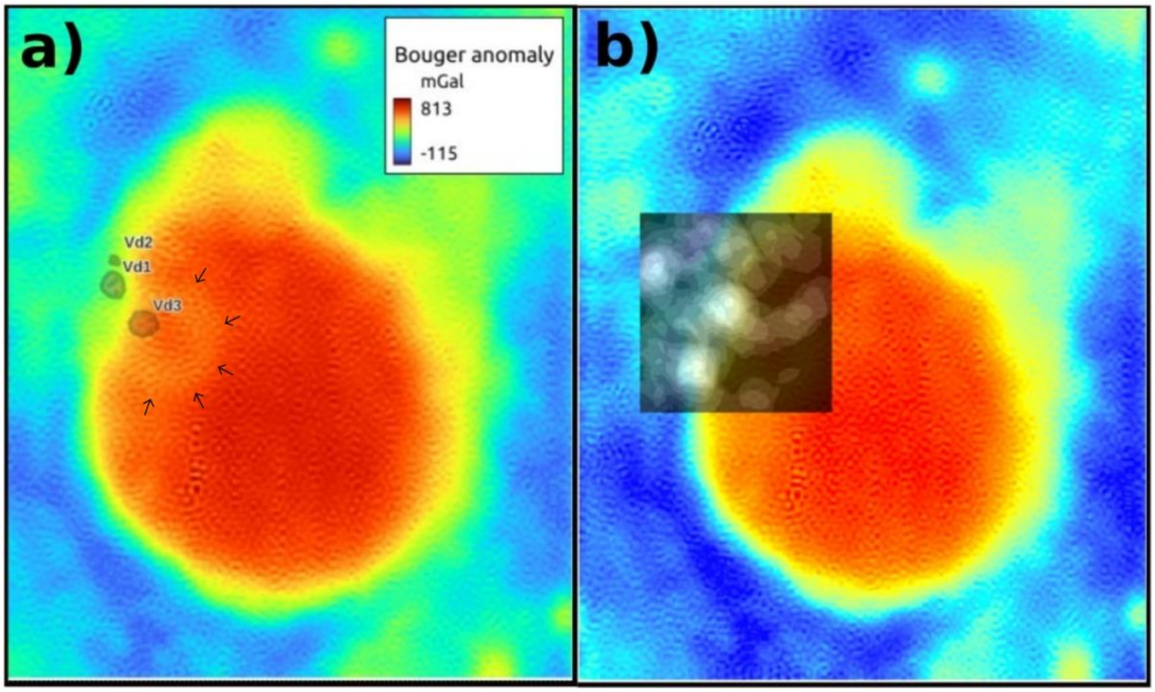

Figure S2. Bouguer anomaly over the Valentine domes. a) The mare has a strong positive anomaly, but a ring-shaped structure with a lower anomaly is located near to the domes (black arrows). The position of the three domes is shown. b) Line density of the zone, lineaments are concentrated in the rim of the basin and the domes. The underlying structure might be a buried crater, which could have weakened the crust more in this location, allowing the emplacement of the intrusive system.

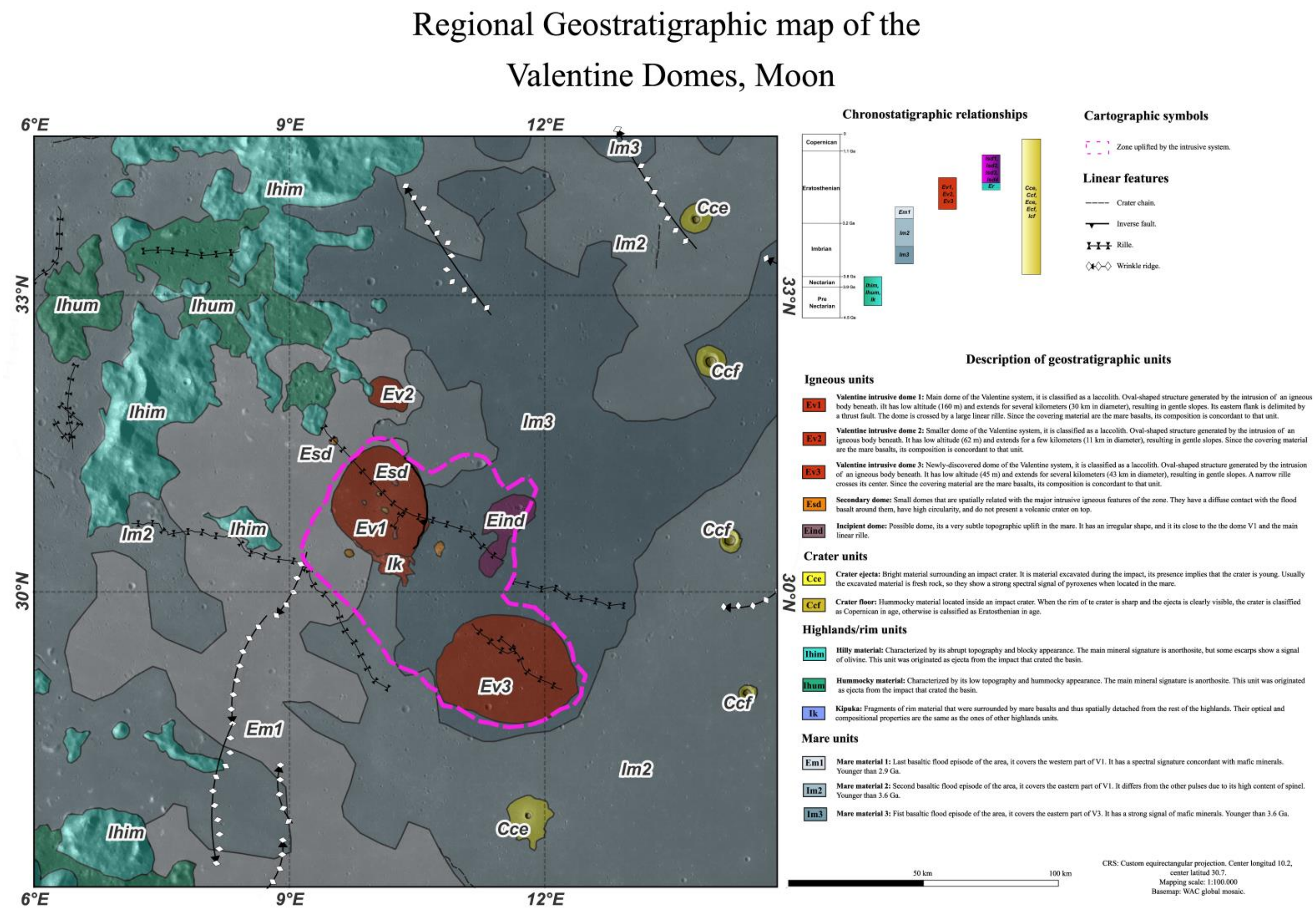

Figure S3. Regional geostratigraphic map of the Valentine domes system.

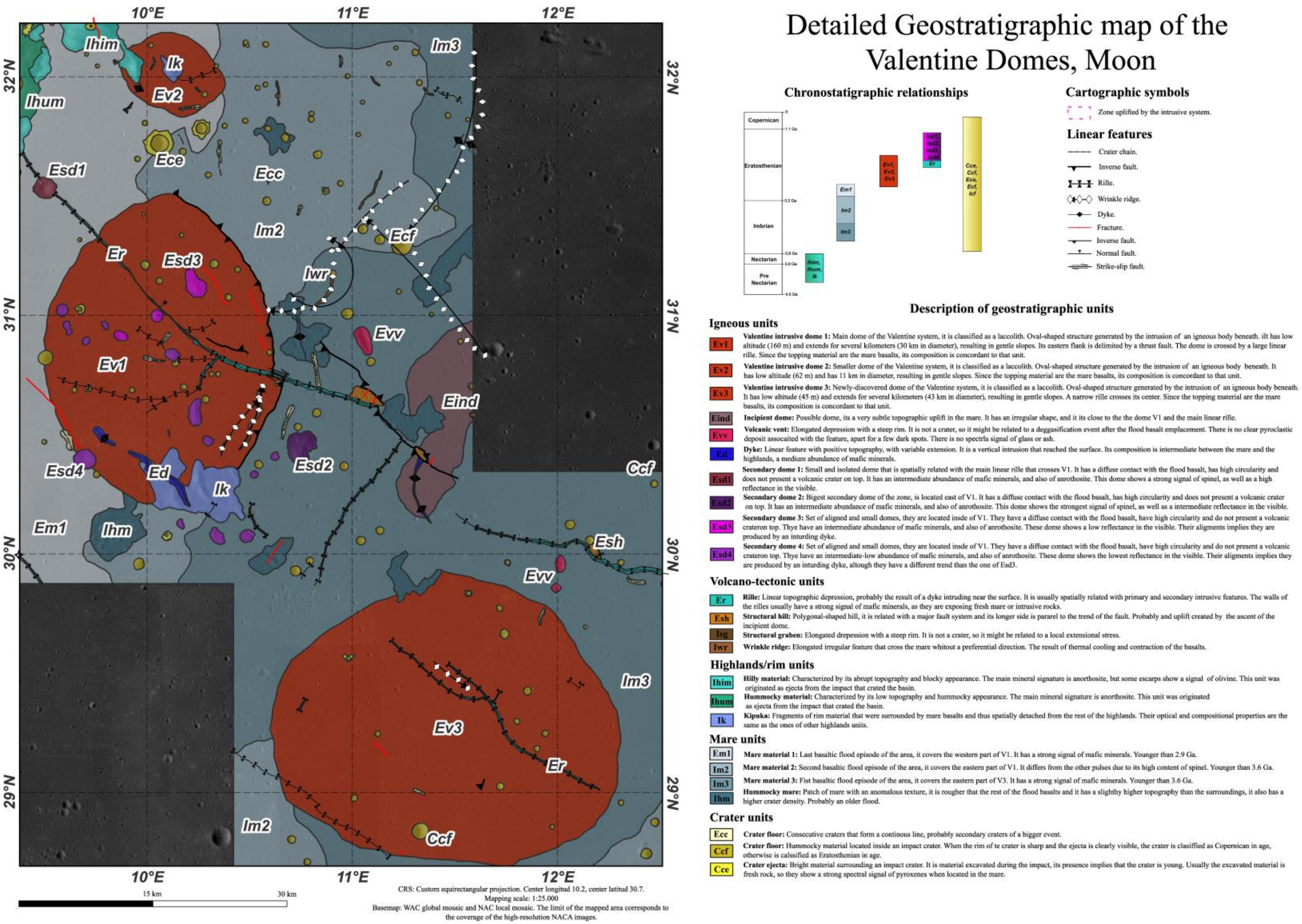

Figure S4. Detailed geostratigraphic map of the Valentine domes system.

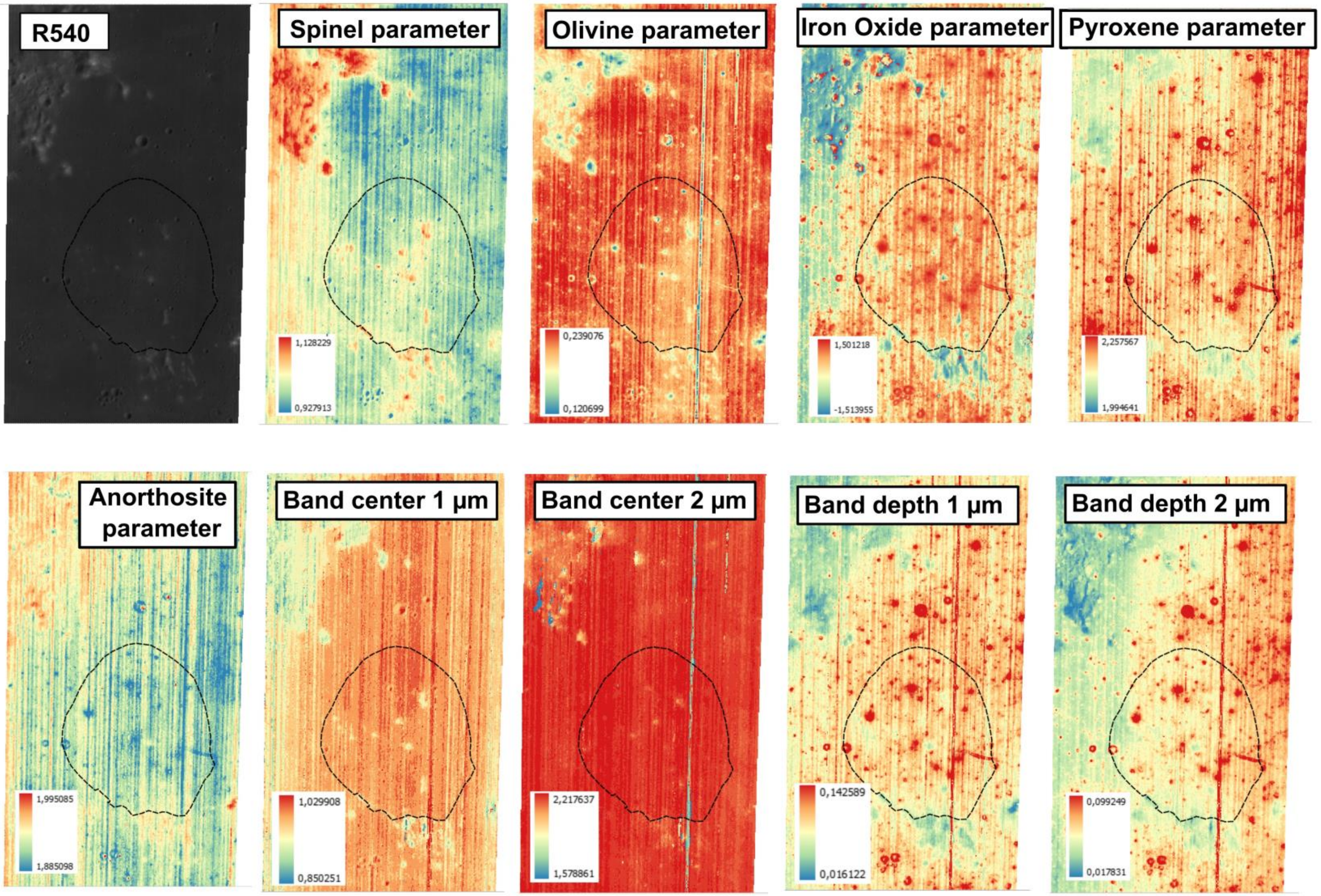

R540
Spinel parameter
1,128229
0,927913
Olivine parameter
0,239076
0,120699
Iron Oxide parameter
1,501218
-1,513955
Pyroxene parameter
2,257567
1,994641
Anorthosite parameter
1,995085
1,885098
Band center 1 μm
1,029908
0,850251
Band center 2 μm
2,217637
1,578861
Band depth 1 μm
0,142589
0,016122
Band depth 2 μm
0,099249
0,017831

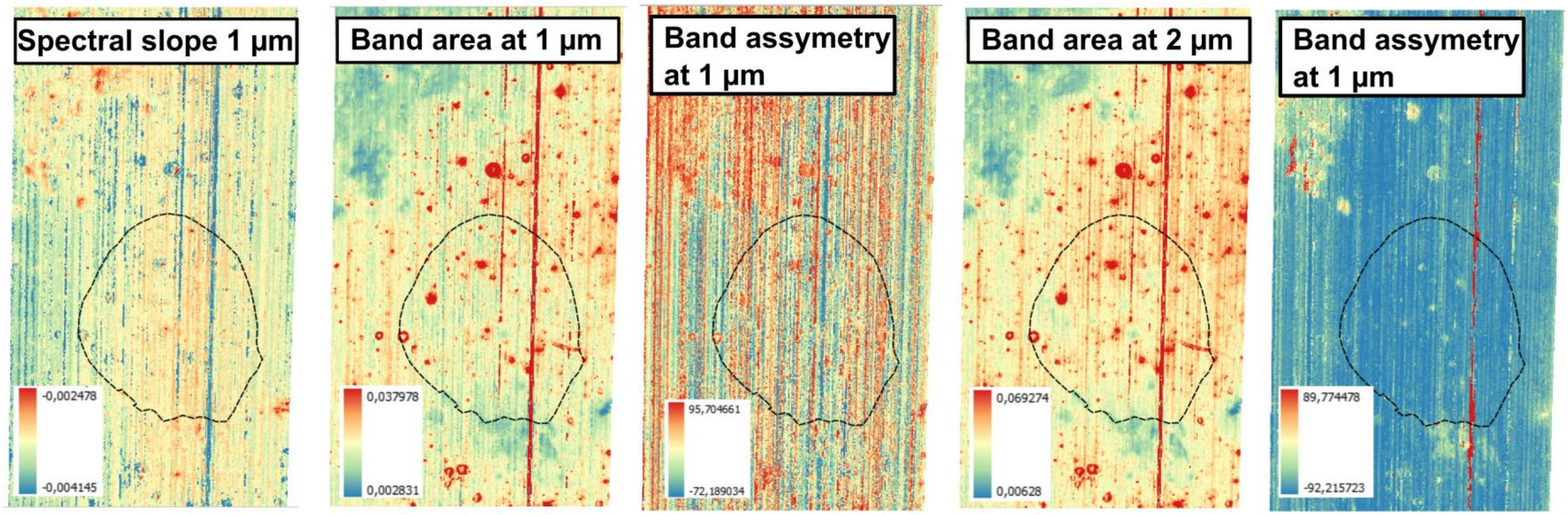

Figure S5. Spectral indexes derived from M^3.